

การศึกษาโครงสร้างของผลึกนาโน ZnO ที่เจือด้วย S
โดยกระบวนการออกซิเดทีฟแอนเนียลิ่ง

นางรัตติยา งามชัยภูมิ

วิทยานิพนธ์นี้เป็นส่วนหนึ่งของการศึกษาตามหลักสูตรปริญญาวิทยาศาสตรมหาบัณฑิต
สาขาวิชาฟิสิกส์
มหาวิทยาลัยเทคโนโลยีสุรนารี
ปีการศึกษา 2552

**STRUCTURAL INVESTIGATION OF
S-DOPED ZnO NANOCRYSTALS PREPARED
BY OXIDATIVE ANNEALING**

Rattiya Ngonchaiyaphum

A Thesis Submitted in Partial Fulfillment of the Requirements for the

Degree of Master of Science in Physics

Suranaree University of Technology

Academic Year 2009

**STRUCTURAL INVESTIGATION OF S-DOPED ZnO
NANOCRYSTALS PREPARED BY OXIDATIVE
ANNEALING**

Suranaree University of Technology has approved this thesis submitted in partial fulfillment of the requirements for the Degree of Master of Science.

Thesis Examining Committee

(Assoc. Prof. Dr. Prapun Manyum)

Chairperson

(Dr. Saroj Rujirawat)

Member (Thesis Advisor)

(Prof. Dr. Sukit Limpijumnong)

Member

(Asst. Prof. Dr. Prayoon Songsiriritthigul)

Member

(Prof. Dr. Sukit Limpijumnong)

Vice Rector for Academic Affairs

(Assoc. Prof. Dr. Prapun Manyum)

Dean of Institute of Science

รัตติยา กองชัยภูมิ : การศึกษาโครงสร้างของผลึกนาโน ZnO ที่เจือด้วย S โดยกระบวนการออกซิเดทีฟแอนเนียลลิ่ง (STRUCTURAL INVESTIGATION OF S-DOPED ZnO NANOCRYSTALS PREPARED BY OXIDATIVE ANNEALING) อาจารย์ที่ปรึกษา : อาจารย์ ดร.สาโรช รุจิรวรรณ, 76 หน้า.

ZnS และ ZnO เป็นสารประกอบกึ่งตัวนำที่มีช่องว่างแถบพลังงานกว้าง ซึ่งนิยมนำมาประยุกต์ใช้เป็นอุปกรณ์ตัวนำโปร่งแสงและทัศนอุปกรณ์อิเล็กทรอนิกส์ เนื่องจากสารประกอบทั้งสองมีค่าช่องว่างแถบพลังงานแตกต่างกัน หากสามารถทำการสังเคราะห์สารประกอบผสมนี้ให้สามารถควบคุมแถบความต่างของพลังงานได้ จะทำให้มีการประยุกต์ใช้ในวิศวกรรมช่องว่างแถบพลังงานบนสารประกอบตระกูล ZnO-ZnS ได้ ในการศึกษาครั้งนี้ จึงได้เสนอวิธีการออกซิเดทีฟแอนเนียลลิ่ง เพื่อใช้ในการสังเคราะห์สารประกอบผสมทั้งสองนี้ โดยมีสมมุติฐานในการเจือปนกันของธาตุในรูปของ ZnS_xO_{1-x} ซึ่งกระบวนการออกซิเดทีฟแอนเนียลลิ่งที่ใช้อาจทำให้เกิดมีอะตอม S ตกค้างอยู่ในสารประกอบดังกล่าวได้ เพื่อที่จะยืนยันสมมุติฐานดังกล่าว ในการศึกษาครั้งนี้ จึงได้ใช้เทคนิคสเปกโทรสโกปีการดูดกลืนรังสีเอกซ์ ณ สถาบันวิจัยเครื่องกำเนิดแสงซินโครตรอนแห่งชาติ ร่วมกับการใช้เครื่องมือวิเคราะห์แบบมาตรฐานต่างๆ ที่มีอยู่ในมหาวิทยาลัยเทคโนโลยีสุรนารี ในการวิเคราะห์โครงสร้างในระดับจุลภาคของสารประกอบที่สังเคราะห์ขึ้น และนำผลไปเปรียบเทียบกับสเปกตรัมที่ได้จากการคำนวณ

จากการศึกษาโครงสร้างของ ZnO:S ที่ผ่านกระบวนการออกซิเดทีฟแอนเนียลลิ่ง พบการเปลี่ยนแปลงโครงสร้างจากลูกบาศก์แบบซิงค์เบลนด์ ของ ZnS ไปเป็นเฮกแซกโกนอลแบบเวอร์ทไฮท์ ของ ZnO ที่อุณหภูมิประมาณ 600°C เมื่อทำการศึกษาด้วยกล้องจุลทรรศน์อิเล็กตรอนแบบส่องกราดพบพื้นผิวของกลุ่มผลึกมีลักษณะขรุขระเป็นรูพรุนเพิ่มมากขึ้นเมื่อใช้อุณหภูมิของการแอนเนิลเพิ่มขึ้น โดยพบว่าปริมาณของ S ได้ลดลงเหลือประมาณ 0.25% ที่อุณหภูมิ 800°C และเมื่อทำการศึกษาโดยใช้วิธีการเลี้ยวเบนรังสีเอกซ์ พบการเปลี่ยนแปลงโครงสร้างผลึกจาก ZnS เป็น ZnO ที่อุณหภูมิ 600°C - 700°C และผลึกมีขนาดใหญ่ขึ้นเมื่ออุณหภูมิของการเผาเพิ่มสูงขึ้น โดยมีขนาดเม็ดผลึกประมาณ 30 - 80 nm ซึ่งสอดคล้องกับการศึกษาโดยใช้กล้องจุลทรรศน์อิเล็กตรอนแบบส่องผ่าน และการศึกษาด้วยวิธีการเลี้ยวเบนลำอิเล็กตรอน

เมื่อทำการวิเคราะห์โครงสร้างของ ZnO:S ที่ผ่านกระบวนการออกซิเดทีฟแอนเนียลลิ่ง โดยใช้เทคนิคสเปกโทรสโกปีการดูดกลืนรังสีเอกซ์ โดยการวัดที่ Zn K-edge พบว่าสารประกอบหลังจากเผาที่อุณหภูมิ 600°C - 800°C มีโครงสร้างผลึกเหมือนกับ ZnO แต่เมื่อทำการวัดที่ S K-edge พบว่าอะตอม S ส่วนใหญ่วางตัวอยู่ในโครงสร้าง $(SO_4)^{2-}$ และจากการวิเคราะห์โครงสร้างด้วย

EXAFS ให้ระยะพันธะ S-O เฉลี่ยประมาณ 1.5 Å ผลการทดลองแสดงให้เห็นว่าวัสดุดังกล่าวประกอบด้วยผลึกนาโน ZnO ที่มี $(\text{SO}_4)^{2-}$ แทรกอยู่และไม่ใช่สารประกอบของ $\text{ZnS}_x\text{O}_{1-x}$ แต่อย่างไร

RATTIYA NGONCHAIYAPHUM : STRUCTURAL INVESTIGATION
OF S-DOPED ZnO NANOCRYSTALS PREPARED BY OXIDATIVE
ANNEALING. THESIS ADVISOR : SAROJ RUJIRAWAT, Ph.D.
76 PP.

ZnO and ZnS are wide-bandgap semiconductors that have been widely used in transparent conductors and optoelectronic devices. Due to different bandgap values the alloys of both semiconductors may give an opportunity for bandgap engineering on ZnO-ZnS family. In this study, the oxidative annealing technique is proposed to synthesize alloys of the two compounds, with the assumption that the process may leave some sulfur atoms in the annealed compounds and result in $\text{ZnS}_x\text{O}_{1-x}$. This assumption was verified by using x-ray absorption spectroscopy (XAS) facility of the Synchrotron Light Research Institute and the other standard analytical instruments available at Suranaree University of Technology for microstructural investigations of the annealed products.

For ZnO:S samples prepared by oxidative annealing, it was found that the crystal structure changes from cubic zincblend of ZnS to hexagonal wurtzite of ZnO occurs when the annealing temperature is greater than 600°C. Scanning electron microscope showed that the surface roughening of product powder increased together with the annealing temperature. Sulfur was found to be approximately 0.25% in 2 h, 800°C annealed products. With x-ray diffraction, it can be concluded that the change of crystal structure from ZnS to ZnO occurs at the temperature between 600°C - 700°C. The crystal grain size increased with annealing temperature to be in the range of 30 - 80 nm. The results agreed well with the measurements from transmission electron microscope and electron diffraction.

The study of oxidative annealed ZnO:S products by XAS on Zn *K*-edge showed that after annealing at 600°C - 800°C the compounds contain a similar structure to that of ZnO. However, from S *K*-edge measurement, it was found that the majority of sulfur are in the form of $(\text{SO}_4)^{2-}$ after annealing. The EXAFS analysis showed that the averaged S-O distance is approximately 1.5 Å. These experimental results showed that that the samples are mainly ZnO nanocrystals with $(\text{SO}_4)^{2-}$ contaminant but not $\text{ZnS}_x\text{O}_{1-x}$ alloys.

ACKNOWLEDGEMENTS

This thesis could not have been completed without the help and support of many people. I would like to thank Dr. Saroj Rujirawat, my thesis advisor, for his patient guidance, advices, and encouragement throughout my master study, Assoc. Prof. Dr. Prapun Manyum, Prof. Dr. Sukit Limpijumnong, Asst. Prof. Dr. Prayoon Songsiriritthigul for serving as the thesis examining committee. Asst. Prof. Dr. Chinorat Kobdaj, Assoc. Prof. Dr. Puangratana Pairor, and all academic members of the School of Physics would be the next group of people who I would like to convey my appreciation for giving their time to suggest, express kindness throughout my study.

I would like to acknowledge all staff members of the Center for Scientific and Technological Equipment, Suranaree University of Technology, and Synchrotron Light Research Institute for their helps in operating equipments during specimen characterizations. Furthermore, I would like to thank all graduate students at the School of Physics, for their hospitality and being my good friends.

Finally, I would like to express my gratitude to my parents, my husband and my son for their infinite love, understanding, encouragement and taking a good care of me throughout my studies.

Rattiya Ngonchaiyaphum

CONTENTS

	Page
ABSTRACT IN THAI	I
ABSTRACT IN ENGLISH	III
ACKNOWLEDGEMENTS	V
CONTENTS	VI
LIST OF TABLES	VIII
LIST OF FIGURES	IX
LIST OF ABBREVIATIONS	XIII
CHAPTER	
I INTRODUCTION	1
1.1 Background	1
1.2 Review of Literatures	4
1.2.1 Background on zinc oxide	4
1.2.2 Background on zinc sulfide	5
1.2.3 Bandgap engineering of ZnS-ZnO	6
1.2.4 Synthesis of ZnO:S	7
1.3 Research objective	10
1.4 Scope and limitation of the study	10
II RESEARCH METHODOLOGY	11
2.1 Oxidative annealing	11
2.1.1 Preparation of S-doped ZnO	11
2.2 X-ray powder diffractometry (XRD)	12

CONTENTS (Continued)

	Page
2.3 Thermogravimetric analysis (TGA)	15
2.4 Scanning electron microscope (SEM)	20
2.5 Transmission electron microscope (TEM)	25
2.6 X-ray absorption spectroscopy (XAS)	33
2.6.1 X-ray absorption near-edge structure (XANES)	35
2.6.2 Extended x-ray absorption fine structure (EXAFS)	37
2.7 X-ray absorption spectroscopy experimental set up	40
III STANDARD CHARACTERIZATION RESULTS AND DIS-	
CUSSION	43
3.1 Oxidative annealing	43
3.2 X-ray diffraction (XRD)	44
3.3 Thermal gravitational analysis (TGA)	49
3.4 Scanning electron microscope (SEM)	50
3.5 Energy Dispersive Spectroscopy (EDS)	52
3.6 Transmission electron microscope (TEM)	53
IV XAS STUDY OF SULFUR DOPED ZINC OXIDE	58
4.1 XAS measurement of sulfur doped ZnO	58
4.2 XANES Analysis	59
4.3 EXAFS Analysis	61
V CONCLUSIONS	67
REFERENCES	68
APPENDIX	73
CURRICULUM VITAE	76

LIST OF TABLES

Table	Page
1.1	Some properties of zinc sulfide and zinc oxide. 6
3.1	The mean crystal grain size of ZnS powder and ZnO:S annealing products at 200°C - 800°C calculated from Debeye-Scherrer formula. 46
3.2	The assigned (<i>h k l</i>) indices for group I (ZnS) $2d_{hkl} \sin \theta = n\lambda$ and $d_{hkl} = \frac{a}{\sqrt{h^2+k^2+l^2}}$ 47
3.3	Calculation of lattice parameter for the XRD peaks group I (ZnS). 48
3.4	The assigned (<i>h k l</i>) from non-cubic crystal group II (ZnO:S) $\frac{1}{d^2} = \frac{4}{3} \left(\frac{h^2+hk+k^2}{a^2} \right) + \frac{l^2}{c^2} = \frac{4 \sin^2 \theta}{\lambda^2}$ 49
3.5	Calculated lattice parameters for XRD group II (ZnO:S) $\frac{1}{d^2} = \frac{4}{3} \left(\frac{h^2+hk+k^2}{a^2} \right) + \frac{l^2}{c^2} = \frac{4 \sin^2 \theta}{\lambda^2}$ 49
3.6	The sulfur concentrations in annealing products as determined by EDS. 53
4.1	Results from the EXAFS fitting for S-O bonds in ZnO:S nanocrystals compared to ZnSO ₄ : R_0 is nearest neighbor shell distance, N is coordination number, σ^2 is Debye-waller factor, and R-factor is the residue. 66

LIST OF FIGURES

Figure		Page
1.1	Crystal structure of ZnO (wurtzite).	4
1.2	Structure of zinc sulfide (zincblend).	5
1.3	Plot of band gap and II-VI bond length of ZnS and ZnO (www.iic.kyoto-u.ac.jp).	7
2.1	Flow chart of the preparation procedure for S-doped ZnO.	12
2.2	The X-ray diffraction beam path.	13
2.3	Schematic illustration of $\theta - 2\theta$ x-ray diffraction experiment [adapted from (Smith et al., 2007)].	15
2.4	Schematic representation of X-ray diffractometer D5005 [adapted from (BRUKER, Analytical X-ray Systems, 1998)].	16
2.5	XRD experimental set up at the Center of Science Technology Equipment.	16
2.6	Schematic diagram of TGA; (a) Sensor and Thermocouple Details and (b) Balance and Furnace Components (TA Instruments, Inc., 2000).	18
2.7	The main parts of DSC-TGA (Model SDT 2960): 1) Sample and reference balance assemblies, which provide the precise measure- ment of heat flow and sample weight. 2) Furnace, which controls the sample atmosphere and temperature and 3) The cabinet, where the system electronics and mechanics are housed.	19
2.8	DSC and TGA data of ZnS powder.	20

LIST OF FIGURES (Continued)

Figure		Page
2.9	Schematic diagram of signals in SEM.	21
2.10	SEM micrograph of S-doped ZnO powder.	22
2.11	Principles schematic illustration of SEM (JEOL, Ltd., 1989).	23
2.12	Schematic diagram of an EDS.	25
2.13	(a) Cross section of column in TEM (JEOL, Ltd., 1996) and (b) Transmission electron microscopy JEOL JEM-2010.	28
2.14	Ray diagrams of (a) diffraction pattern and (b) image [adapted from (William and Carter, 1996)].	31
2.15	Graphical representation of geometry of Bragg's Law [adapted from (Hammond, 1992)].	32
2.16	Creation of diffraction pattern (a) reciprocal space lattice planes and (b) detector face on view [adapted from (Hammond, 1992)].	32
2.17	Schematic view of x-ray absorption measurement in transmission mode.	34
2.18	The relationship between the energy transitions and absorption edges [adapted from (Rehr and Albers, 2000)].	35
2.19	Normalize Zn <i>K</i> -edge absorption spectra classified into two regions, XANES and EXAFS.	35
2.20	Schematic of the radial portion of the photoelectron wave.	38
2.21	The three modes of XAS measurement (a) transmission mode, (b) fluorescence mode and (c) electron yield. [adapted from (Kawai, 2000)].	40

LIST OF FIGURES (Continued)

Figure	Page
2.22	.Schematic illustration of the experimental setup of transmission-mode X-ray absorption spectroscopy 41
2.23	.XAS experimental set up at the Siam Photon Laboratory, Synchrotron Light Research Institute 41
2.24	The excited state (a) x-ray fluorescence and (b) the Auger effect. [adapted from (Koningsberger and Prins, 1998)]. 42
3.1	ZnS powder and ZnO:S annealing products. 45
3.2	XRD patterns of ZnS and annealing products. 46
3.3	XRD patterns of ZnS powder and annealing products from 200°C - 500°C. 47
3.4	XRD patterns of ZnO:S annealing products at 600°C - 800°C. . . . 48
3.5	TGA data of ZnS annealing. 50
3.6	SEM images of ZnS powder and annealing products at 200°C - 800°C. 51
3.7	EDS spectra of (a) ZnS powder, (b) 600°C S-doped ZnO powder and (c) 800°C S-doped ZnO powder. 52
3.8	TEM images of ZnS powder and annealing product at 200°C and (b) selected area electron diffraction patterns of ZnS powder and annealing product at 200°C. 54
3.9	(a) TEM images of annealing products at 300°C, 400°C and 500°C and (b) selected area electron diffraction patterns of annealing products at 300°C, 400°C and 500°C. 55

LIST OF FIGURES (Continued)

Figure	Page
3.10	(a) TEM images of annealing products at 600°C, 700°C and 800°C and (b) selected area electron diffraction patterns of annealing products at 600°C, 700°C and 800°C. 56
3.11	The indexed electron diffraction patterns of (a) annealing product at 200°C (ZnS) and (b) 600°C (ZnO:S). 57
4.1	Zn <i>K</i> -edge XANES spectra of in ZnO:S annealed at different temperatures compared with ZnO and ZnS. 59
4.2	S <i>K</i> -edge XANES spectra of in ZnO:S annealed at different temperatures compared with ZnSO ₄ and ZnS. 60
4.3	k ² -weighted Zn <i>K</i> -edge EXAFS spectra (dot lines): ZnS powder, annealing products at 200°C - 800°C, and pure ZnO powder. Fittings spectra are shown in dash lines. The FEFF-generated spectra are shown in solid lines. 62
4.4	Real space Zn <i>K</i> -edge EXAFS spectra (solid): ZnS powder, annealing products at 200°C - 800°C, and pure ZnO powder. Fittings spectra are shown in dash lines. 63
4.5	k ² -weighted S <i>K</i> -edge EXAFS spectra (dot lines): ZnS powder, annealing products at 200°C - 800°C, and pure ZnSO ₄ powder. Fittings spectra are shown in dash lines. The FEFF-generated (SO ₄) ²⁻ spectrum is shown in solid line. 64
4.6	Real space S <i>K</i> -edge EXAFS spectra (solid): ZnS powder, annealing products at 200°C - 800°C, and pure ZnSO ₄ powder. 65

LIST OF ABBREVIATIONS

XRD	X-ray diffraction
IR	Infrared spectroscopy
NMR	Nuclear magnetic resonance
TGA	Thermal gravitation analysis
SEM	Scanning electron microscope
EDS	Energy dispersive spectroscopy
TEM	Transmission electron microscope
ED	Electron diffraction
XAS	X-ray absorption spectroscopy
XANES	X-ray absorption near edge structure
EXAFS	Extended x-ray absorption fine structure
SUT	Suranaree University of Technology
SLRI	Synchrotron Light Research Institute
FEFF	Effective scattering amplitude
FWHM	Full width at half maximum
RT	Room temperature
HRTEM	High Resolution Transmission Electron Microscopy
SEAD	Selected area electron diffraction
LPE	Liquid phase epitaxy
MBE	Molecular beam epitaxy

LIST OF ABBREVIATIONS (Continued)

CVD	Chemical vapor epitaxy
RF	Radio frequency
PL	Photoluminescence
SE	Secondary electrons
BSE	Back scattered electrons
MCA	Multi channel analyzer
CCD	Charge coupled device
CRT	Cathode ray tube

CHAPTER I

INTRODUCTION

1.1 Background

It is generally excepted that research and development in new materials, especially in semiconductors, helps transforming the world into the present form. In the early days, researchers have focused their works on elemental semiconductors such as silicon (Si) and germanium (Ge) (Jagadish and Pearton, 2006). Based on the well established theory described in text book, the research and development in elemental semiconductor have gained tremendous success. The breakthroughs in silicon technology have started revolutions in the electronics industry. Today, the computer and information technology industries are mostly relying on silicon-based technologies. The Moore's law seems to be continued for a while (Moore, 1965), until the news breakthroughs in nanotechnology bring the world to the new paradigm.

Nevertheless, not long after the beginning of silicon age, it has been realized that other semiconductors also possess excellent properties suitable for electronic applications. For example, the optoelectronics devices could be made from direct bandgap, compound semiconductors, which energy gap E_g could be tailor-made. High power applications need high break down voltage properties to withstand the high electric field. Solid state lighting could consume less energy than the incandescent light bulb. Hence, research and development in new semiconductors still continue to grow.

In the recent years, the wide band gap compound semiconductors have

attracted the attention from emerging applications. For example, titanium dioxide (TiO_2) for photo-catalytic applications, gallium nitride (GaN) and zinc oxide (ZnO) for blue light emitters, zinc sulfide (ZnS) for UV detection etc. In application such as, photon detector and photovoltaic cell, the bandgap of material must be engineered to match the energy of absorbing photon. The word "bandgap engineering" was coined to call the process that can the band gap of by controlling the composition of certain semiconductor alloys (Makino et al., 2001). The Vegard's law states that there is a linear relation between lattice constant and composition of a solid solution at constant temperature. The same law could be extended to establish the relation between E_g and composition of semiconductors. The Vegard's law was shown to be applicable for a certain range of semiconductor families (Fong et al., 1976). Base on this empirical law, bandgap engineering has been practiced, very successfully, in many families of compound semiconductors such as gallium aluminum arsenide (GaAlAs) for laser diode and high speed transistor, gallium indium nitride (GaInN) for blue light emitter and mercury cadmium telluride (HgCdTe) for infrared detection applications.

To perform bandgap engineering, one must find a way to form solid alloys of semiconductors with desired composition. There are several methods to synthesis such alloys, i.e. bulk crystal growth, liquid phase epitaxy (LPE), molecular beam epitaxy (MBE), chemical vapor epitaxy (CVD), sputtering (Gupta and Mansingh, 1996). In general, the equipments to be used for alloying semiconductor compounds could be accessible only in well-equipped laboratories. It is also true that operation and maintenance of those equipments require some funding and manpower resources. Those requirements raise the cost of alloyed products effectively. If an economic way can be used for alloying semiconductors, it would be beneficial to the some researchers in academic institutions who want to pursue

compound semiconductor research experiment with very limited budget (which is the general case for Thailand).

From the fact that, all of us live in the earth atmosphere: nitrogen, oxygen, and carbon can be found in atmosphere. Oxygen is a column IV of the periodic table and can be obtained with no cost and the oxidation process could occur easily. When we thermally anneal a compound semiconductor in air, the powder could be oxidized and results in new product.

In this thesis, we used a method called “oxidative annealing” or “thermal oxidation” to explore the possibility of alloying ZnS with ZnO to get “S-doped” ZnO or ZnO:S.

There are many characterization techniques capable for microscopic study of compound semiconductor and non crystalline materials, i.e. x-ray diffraction (XRD), infrared spectroscopy (IR), nuclear magnetic resonance (NMR) and transmission electron microscope (TEM). However, the diffraction techniques using periodic nature of material may not be used effectively on studying the microstructure around the impurities in semiconductor materials, the components are randomly distributed. Nonetheless, x-ray absorption spectroscopy (XAS) has been shown to be an efficient way to verify the microstructure of alloys and compound semiconductor materials (Rehr and Albers, 2000).

In this thesis, characterization techniques, available locally in Suranaree University of Technology, (SUT) and Synchrotron Light Research Institute (Public Organization), (SLRI), were used to investigate the microstructural properties of the resulting products. In particular, XAS was employed to study the microstructure of S-doped ZnO nanocrystals prepared by oxidative annealing. The results obtained are unique and can not be obtained by using standard characterization techniques.

1.2 Review of Literatures

1.2.1 Background on zinc oxide

Zinc oxide is a wide bandgap compound semiconductor ($E_g = 3.37$ eV) with chemical formula ZnO. It occurs as white hexagonal “wurtzite” crystal or a white powder commonly known as zinc white. The crystal structure of ZnO is shown in Figure 1.1.

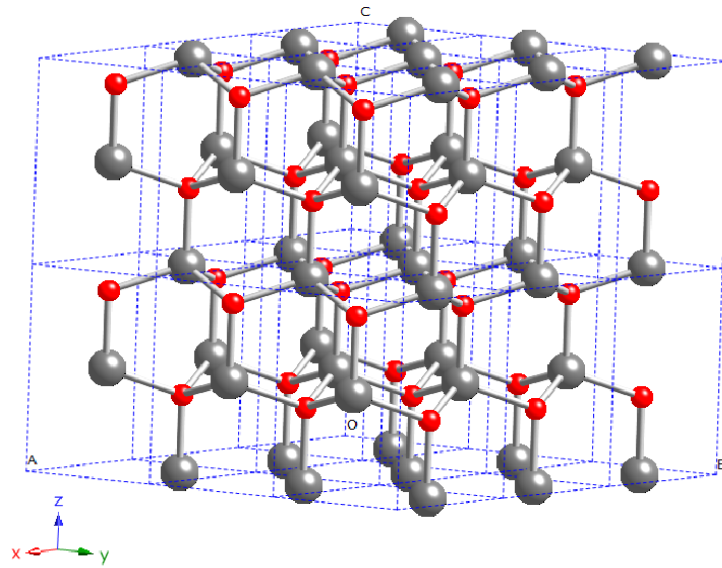


Figure 1.1 Crystal structure of ZnO (wurtzite).

ZnO is one of the potential materials for low-voltage luminescence and short wavelength light emitter (Wong and Searson, 1999). Due to its high excitonic binding energy of 60 meV, ZnO has high efficient exciton emission at room temperature. It can also be used in surface acoustic wave (SAW) devices (Gorla et al., 1999). In general only n-type ZnO could be consistently produced. The p-type doping of ZnO still be an active research topic of the present day.

ZnO is also one of the promising materials for the realization of nanotech-

nology. The low cost, ZnO in particle forms, are used in a variety of applications such as UV absorption cosmetic powder, antibiotic treatment etc. ZnO micro-engineering structures can also be utilized in photonic devices. For mass production, zinc oxide powders have been synthesized by several methods, such as sol-gel method, solid-state method, gas-phase condensation, liquid-phase chemical precipitation (Yang et al., 2003).

1.2.2 Background on zinc sulfide

Zinc sulfide is also a wide bandgap compound semiconductor with chemical formula ZnS. Its powder has white to yellow color. It is typically encountered in the more stable cubic form ($E_g = 3.54$ eV). The “sphalerite” or “zincblende” cubic crystal structure has been named after this material. The phase transition of zinc sulfide from sphalerite into wurtzite occurs at around 1000°C. The structure of zinc sulfide is shown in Figure 1.2

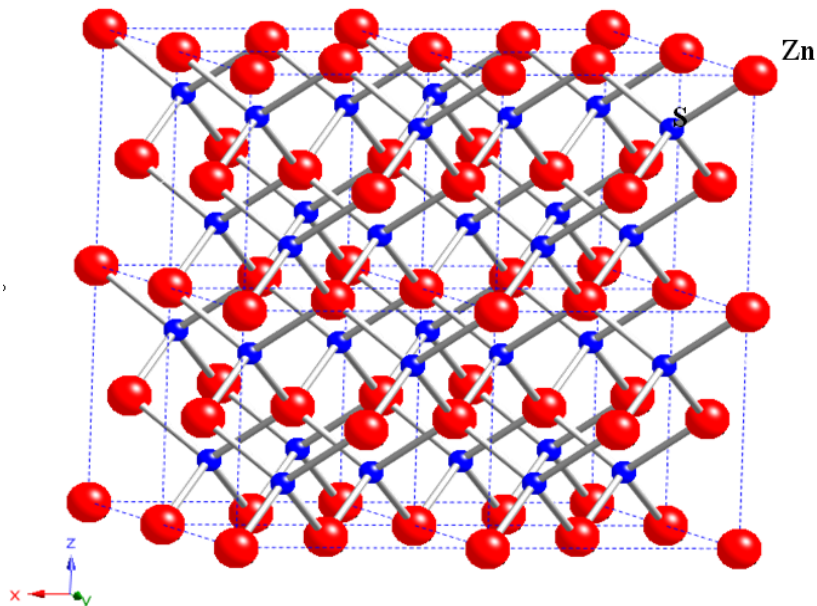


Figure 1.2 Structure of zinc sulfide (zincblende).

Zinc sulfide has received high attention due to its excellent properties, such as large band gap energy, direct recombination and resistance to high electric field. It can be doped as both n-type semiconductor and p-type semiconductor, which is unusual for II-IV semiconductors. Zinc sulfide is a well known phosphor material with various luminescence properties thus it has generally been utilized in the fields of laser, sensors and displays. In the early years of nuclear physics, it was used as a scintillation detector. ZnS emits light on excitation by x-ray or electron beam, making it useful for x-ray and cathode ray screens. Its direct wide band gap offers great potential in optoelectronic applications. Because of its high transmittance it is also used as an optical window, infrared windows or shaped into a lens. Some properties of ZnS and ZnO are compared in Table 1.1.

Table 1.1 Some properties of zinc sulfide and zinc oxide.

	Zinc sulfide	Zinc oxide
Chemical formula	ZnS	ZnO
Structure	Zincblend	Wurtzite
	$a = 5.420\text{\AA}$	$a = 3.248\text{\AA}$, $c = 5.199\text{\AA}$
II-VI bond length	2.42	1.98
Bandgap	3.54 eV	3.37 eV

1.2.3 Bandgap engineering of ZnS-ZnO

Even though, both are II - VI semiconductors, ZnS and ZnO have different crystal structures, one zincblend and the other wurtzite. Therefore, it might not be possible to obtain $\text{ZnS}_x\text{O}_{1-x}$ alloys for a wide range of x . However, if we assume that Vegard's law could be approximately applied for some range of $\text{ZnS}_x\text{O}_{1-x}$ alloys and assume that the alloys with low x have crystal structure similar to ZnO, some properties of S-doped ZnO or ZnO:S may be estimated. A plot between II

- VI bond length and energy gap for ZnO and ZnS is shown in Figure 1.3. From this plot, by following a linear trend, one may guess that $\text{ZnS}_x\text{O}_{1-x}$ could have a higher bandgap than ZnO, i.e. for $\text{ZnS}_{0.1}\text{O}_{0.9}$ would have E_g about 3.4 eV. If $\text{ZnS}_x\text{O}_{1-x}$ alloys could be made, it may find some applications in the UV range.

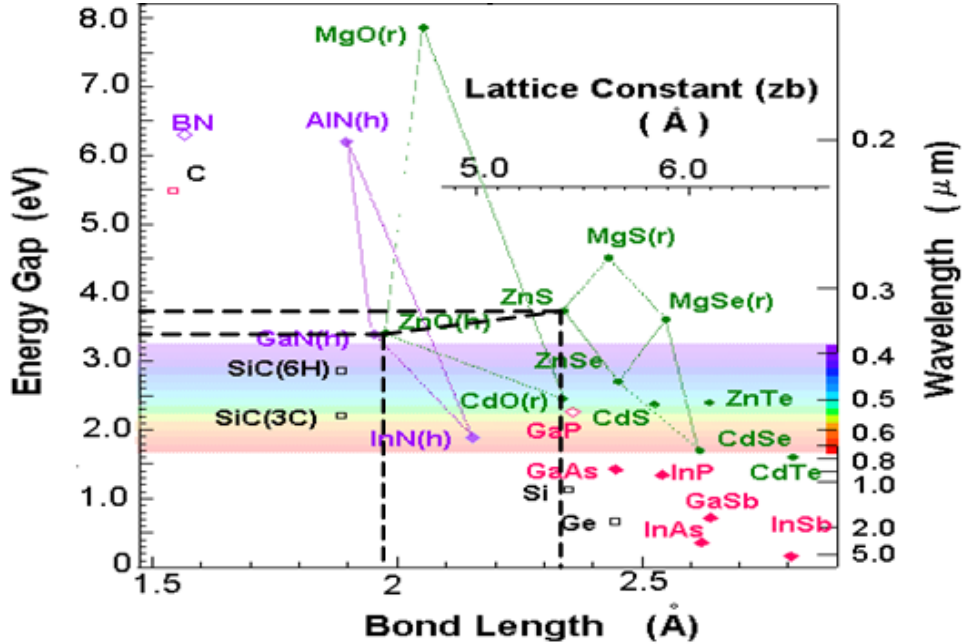


Figure 1.3 Plot of band gap and II-VI bond length of ZnS and ZnO (www.iic.kyoto-u.ac.jp).

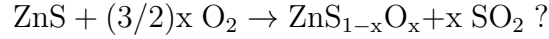
1.2.4 Synthesis of ZnO:S

There are many possible methods to synthesis semiconductor alloys i.e. CVD, MBE, RF sputtering etc. However, most of the techniques require sophisticated synthesis equipments and are not available at SUT, presently. It may be possible to use some simple and economic way to synthesis the material. In this work, we propose to use process called oxidative annealing to explore the possibility of alloying ZnS and ZnO to get either $\text{ZnS}_x\text{O}_{1-x}$ alloys or ZnO:S.

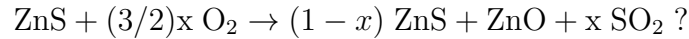
From the fact that, all us live in the earth atmosphere, oxygen can be found freely, the oxidation process could occur easily. When we thermally anneal ZnS in

air, the powder could be oxidized and results in new product. There are several possibilities for the oxidation process.

One of the possible reactions may be:



Some other reaction may be:



The first reaction could allow the formation of $\text{ZnS}_x\text{O}_{1-x}$ while the second reaction would form ZnO domain separately from ZnS domain. Also, the mixture between two processes may be allowed. Another possibility may be the formation of ZnSO_4 product. The investigation of the final product from the annealing experiment may shed the light on the path that the reaction has followed.

Lu et al. have experimentally studied the characteristics of low-temperature synthesized ZnS and ZnO nanoparticles (Lu et al., 2004). They synthesized ZnS nanoparticles by solid-state reaction of zinc acetate and thioacetamide at low temperature. ZnO nanoparticles were obtained after annealing at 600°C in air. The ZnS and ZnO nanoparticles were characterized by x-ray diffraction (XRD), photoluminescence (PL) spectroscopy. They concluded that the mean of the solid-state method, the zinc sulfide nanoparticles have been obtained through the low-temperature synthesis. It was shown the cubic structure and the mean particle size indicates 3.6 nm in diameter in ZnS. After annealed at 600°C in air atmosphere environment, ZnS nanoparticles are oxidized into ZnO nanoparticles. The structure converts from cubic into hexagonal structure. The particle size of ZnO samples calculated from XRD consistent with the TEM image was 37 nm.

Umebayashi et al. have reported that the titanium dioxide (TiO_2) powder doped with sulfur (S) can be synthesized by oxidation annealing of titanium disulfide (TiS_2) powder. TiS_2 turned into anatase TiO_2 when annealed at 600°C . The substitution of S for O was speculated to cause a significant shift in the absorption edge to lower energy (Umebayashi et al., 2002). They concluded that the band gap narrowing of TiO_2 is by S doping. Recently, Smith et al. have experimentally studied the identification of bulk and surface sulfur impurities in TiO_2 using x-ray absorption near edge structure (XANES) (Smith et al., 2007). They have studied sulfur-doped TiO_2 prepared by oxidative annealing of TiS_2 . They have reported good agreement between the measured XANES spectra of Ti and S K -edge and the calculated XANES spectra based on first principles simulations of XANES for S at various locations within TiO_2 . The simulations were performed using the FEFF8 code. From the simulations of pure systems such as TiS_2 and free SO_4 molecule, it was found that the XANES features are in good agreement with the known spectra. For annealing temperature of 300°C or above, the samples are converted to TiO_2 with no detectable TiS_2 phase, according both to XRD and Ti-edge XANES measurements. The S-edge XANES spectrum is found to gradually evolve away from that of TiS_2 . They concluded that the sulfur atoms are mainly on the TiO_2 surface as SO_4 , most likely in the form of split interstitials. The averaged S-O distance was reported to be 1.8 \AA and the next nearest neighbors of the S atom are an O at 2.2 \AA and three Ti at $2.3 - 2.4 \text{ \AA}$ arranged asymmetrically.

In this work, we followed the direction set by Smith et al. (Smith et al., 2007) to investigate the microstructure of ZnO:S by using XAS as the major investigation equipment.

1.3 Research objective

a) To explore the possibility of synthesis $\text{ZnS}_x\text{O}_{1-x}$ alloys by an economic method.

b) To study the conditions of structural phase transformation from ZnS into ZnO.

c) To study the products of oxidative annealed ZnS by characterization tools available in SUT and SLRI. The characterization techniques used in this study are X-ray diffraction (XRD), Thermal gravimetric analysis (TGA), Scanning electron microscope (SEM), Transmission electron microscope (TEM), and X-ray absorption spectroscopy (XAS).

1.4 Scope and limitation of the study

This study is a preliminary research aiming to find an economic way to synthesize $\text{ZnS}_x\text{O}_{1-x}$ II - VI alloys. However, the synthesized products ZnO:S was found to be not in the form of $\text{ZnS}_x\text{O}_{1-x}$. The chemical species of the products were identified using the available tools. Due to the limited beam-time and competitive applications among SLRI users, only a few selected annealing products were characterized by XAS.

CHAPTER II

RESEARCH METHODOLOGY

In this chapter, the research methodology used in this thesis will be reviewed. Firstly, the characterization of ZnO:S products is studied by x-ray diffraction (XRD). Secondly, by the thermal gravitational analysis (TGA), then by scanning electron microscope (SEM), and transmission electron microscope (TEM). Finally, the attention is paid to the local structure around specific atoms which can be done by x-ray absorption spectroscopy (XAS) in both extended x-ray absorption fine structure (EXAFS) and x-ray absorption near-edge structure (XANES). We will describe the general concept of those techniques on how to extract the result from experiments.

2.1 Oxidative annealing

2.1.1 Preparation of S-doped ZnO

Powder zinc sulfide (ZnS) obtained commercially was used as a main starting material without any purification. ZnS powder was annealed in atmosphere at the heating rate of 10°C/min and holding at temperature 200°C - 800°C for 2 hour. The powder was then cooled to 70°C - 90°C for 2 - 4 hour and became fine powder resulting in S-doped ZnO or ZnO:S samples. The procedure is shown in Figure 2.1

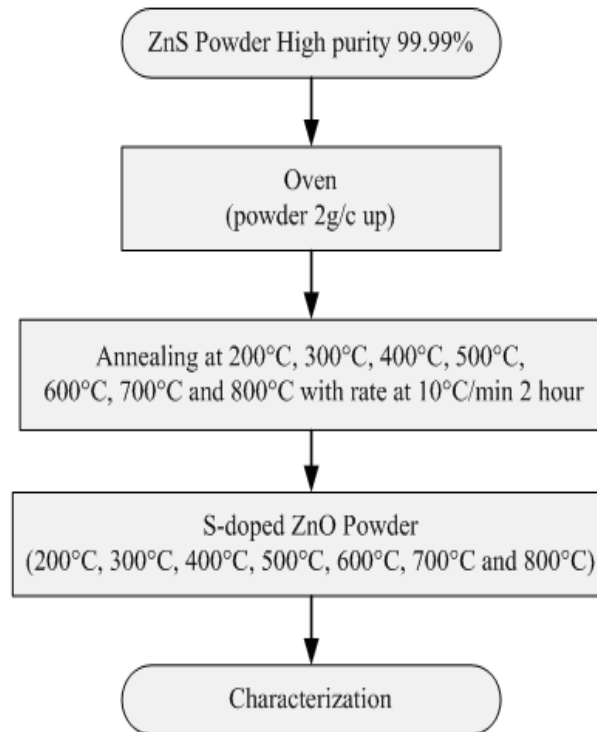


Figure 2.1 Flow chart of the preparation procedure for S-doped ZnO.

2.2 X-ray powder diffractometry (XRD)

X-ray diffraction (XRD) is one of the standard methods that can be used for identify the structure of crystalline solids. In principle XRD measurements come down to measuring distances between lattice planes in the crystal with x-ray plane waves. When the x-ray condition is met, there can be a reflected x-ray, as shown in Figure 2.2. The relationship between the wavelength of x-ray beam, the angle of diffraction θ , and the distance between each set of planes of the crystal lattice, d , is given by Bragg condition

$$2d \sin \theta = n\lambda, \quad (2.1)$$

where, n represents the order of diffraction.

The x-ray diffractometer was used to study crystalline phase identification and can estimate the crystal size of particles. The mean particles size in diameter are purposed by Debye-Scherrer formula

$$D = K\lambda/\beta\cos\theta, \quad (2.2)$$

where D is the mean particle size, λ is the wavelength of X-ray radiation ($\text{CuK}\alpha$ 1.54 Å), β is the full width at half maximum height (FWHM), K is a constant usually taken as 0.89, θ is the diffraction angle.

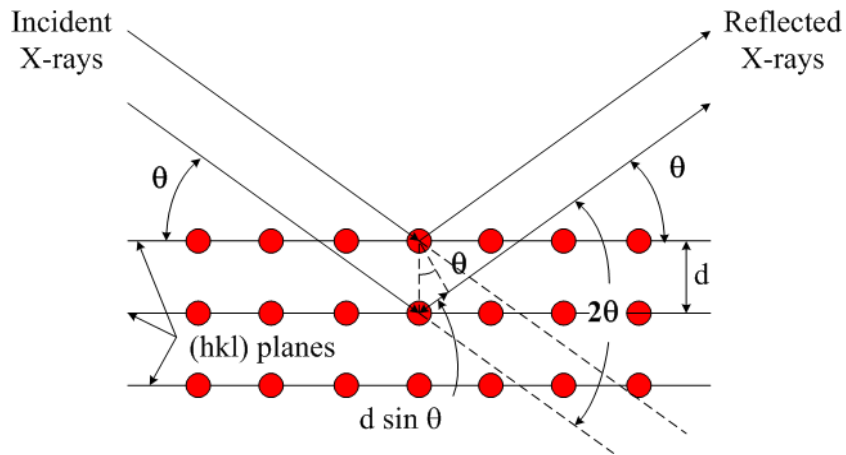


Figure 2.2 The X-ray diffraction beam path.

The Miller's index ($h k l$) can be calculated from Bragg's law:

$$2d_{hkl} \sin \theta = n\lambda, \quad (2.3)$$

and

$$d_{hkl} = \frac{a}{\sqrt{h^2 + k^2 + l^2}}. \quad (2.4)$$

For face center cubic structure, the lattice parameter can be calculated from

$$a_{hkl} = \frac{n\lambda\sqrt{h^2 + k^2 + l^2}}{2\sin\theta}, \quad (2.5)$$

with $\lambda = 1.54\text{\AA}$, $n = 1$. Considering the plane spacing equation for the crystal structure of hexagonal, $(h\ k\ l)$ can be calculated using the lattice parameters from Bravais lattice:

$$\frac{1}{d^2} = \frac{4}{3} \left(\frac{h^2 + hk + k^2}{a^2} \right) + \frac{l^2}{c^2} \quad (2.6)$$

Recall the Bragg's law:

$$\lambda = 2\sin\theta, \quad (2.7)$$

$$\lambda^2 = 4d^2\sin\theta, \quad (2.8)$$

$$\sin^2\theta = \frac{\lambda^2}{4d^2}. \quad (2.9)$$

Combing equation (2.7) and (2.8), we obtain

Hexagonal

$$\frac{1}{d^2} = \frac{4}{3} \left(\frac{h^2 + hk + k^2}{a^2} \right) + \frac{l^2}{c^2} = \frac{4\sin^2\theta}{x^2}. \quad (2.10)$$

Which can be repaired in terms of $\sin^2\theta$ as

$$\sin^2\theta = \left(\frac{\lambda^2}{4} \right) \bullet \left[\frac{4}{3} \left(\frac{h^2 + hk + k^2}{a^2} \right) + \frac{l^2}{c^2} \right], \quad (2.11)$$

where a and c/a are constants for a given diffraction pattern.

The X-ray diffraction experimental is commonly performed by X-ray diffractometer. Actually monochromatic radiation is obtained by reflecting x-ray from

crystal planes. In general, there are four methods of x-ray diffraction technique: Laue Method, Rotating Crystal Method, Debye-Scherrer Powder Method and $\theta - 2\theta$ Diffractometer Method. The schematic diagram of $\theta - 2\theta$ x-ray diffractometer used in this work (BRUKER X-ray diffractometer model D5005 wave length 1.54 Å) is shown in Figures 2.3 and 2.4. The $\theta - 2\theta$ Diffractometer is used for diffraction measurements of unfixed horizontal sample. For this purpose, sample will be rotated to θ and x-ray detector moved to 2θ . The diffraction angle followed on Bragg's equation (2.1). The one-side weight of the tube stand is compensated by a counter weight. Both tube stand and counter weigh are fixed to the outer ring. The picture of actual experimental set up of XRD experimental station at the Center of Science Technology Equipment (CSTE), Suranaree University of Technology is shown in Figure 2.5.

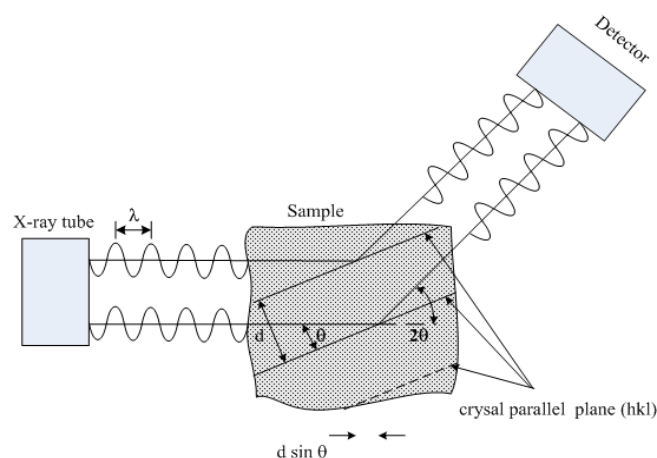


Figure 2.3 Schematic illustration of $\theta - 2\theta$ x-ray diffraction experiment [adapted from (Smith et al., 2007)].

2.3 Thermogravimetric analysis (TGA)

Thermal analysis comprises a group of techniques in which the physical property of the material is measured as a function of temperature while the mate-

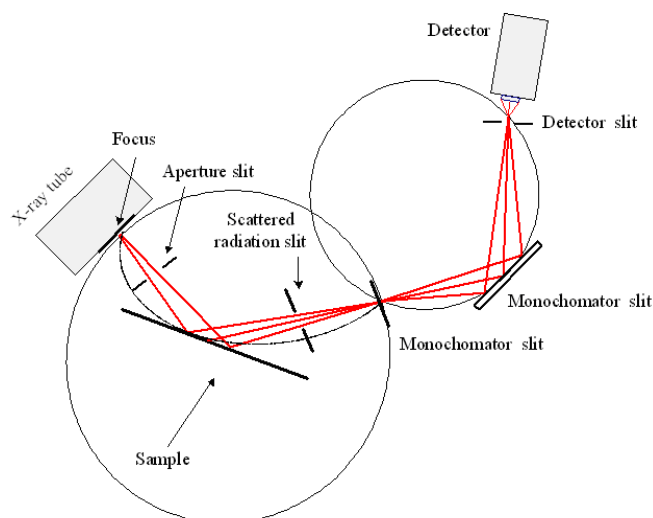


Figure 2.4 Schematic representation of X-ray diffractometer D5005 [adapted from (BRUKER, Analytical X-ray Systems, 1998)].

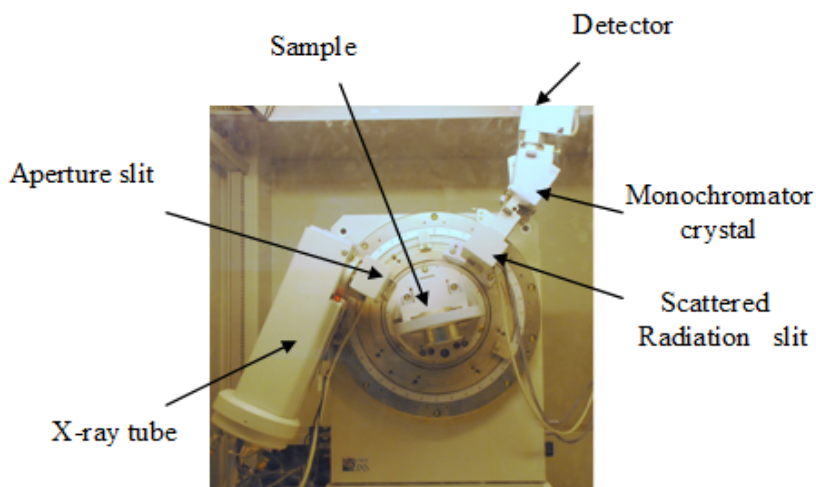


Figure 2.5 XRD experimental set up at the Center of Science Technology Equipment.

rial is exposed to a controlled temperature program. When a sample is heated or cooled at a controlled rate, the weight of a material in an environment is recorded and the change of weight is measured as a function of temperature or time.

Thermal analysis instrument concentrates two thermal analysis techniques:

- 1) Thermogravimetric analysis (TGA), measures the amount and rate of

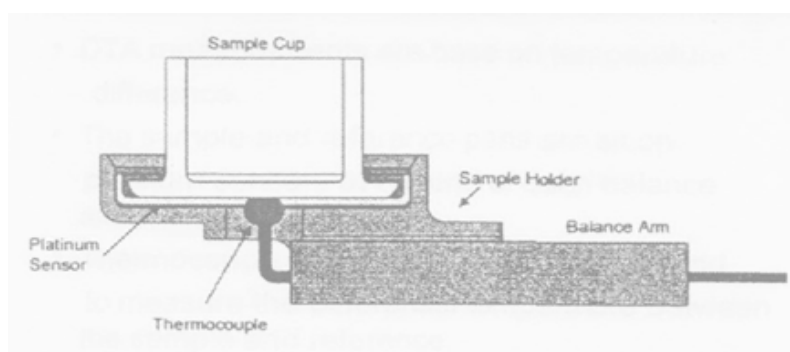
change in sample mass as a function of temperature and time. TGA analysis is used to identify material that shows weight or phase changes as appear of decomposition, dehydration, and oxidation. Two modes are normally used for exploration thermal consistency behavior in controlled atmospheres: (1) dynamic, in which the temperature is increased by follow a linear rate, and (2) isothermal, in which the temperature is kept constant.

2) Differential scanning calorimetry (DSC) measures the thermal flow differences as a sample is uniformly heated as a function of temperature and time. The DSC part of analysis works on the origin that when a sample and an still reference are heated at a known rate in a controlled environment, the increase in the sample and reference temperature will be the same unless a heat-rated change takes place in the sample.

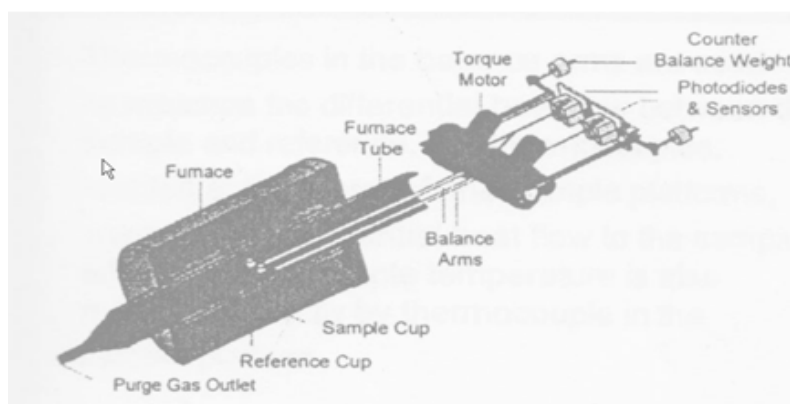
Moreover, executing both DSC and TGA measurements at the same time, on the same tool and same sample, offers greater potency and removes experimental and sampling changeables as factors in the analysis of data.

The thermocouples in the balance arms are used to measure the differential heat flow between the sample and reference. The schematic diagram of a TGA is shown in Figure 2.6. Thermocouples are joined at the center of the sample platforms. Sample temperature is also observed directly by thermocouple in the sample platform. The sample and reference pans are rest on platinum sensors at the end of each balance arms. These pans reach down to platinum sensor. The thermocouples uses a servomotor performed balance system in which the electrical signal from an optical null detector is adapted directly to control the current in a torque motor. When the balance is in null position, a position sensor flag blocks an equal amount of light to each of the photodiodes, as sample weight is lost or increase, the beam becomes derange, causing the unequal amount of light to

strike the photodiodes. The derange signal, called fault signal, is behave upon by the control circuitry and decrease to zero. This is completed by an increase or decrease in the current to the meter movement, causing it to switch back to its original position (null position). The change in current necessary to accomplish this task is directly proportional to the change in mass of the sample. This current is converted to the weight signal.



(a)



(b)

Figure 2.6 Schematic diagram of TGA; (a) Sensor and Thermocouple Details and (b) Balance and Furnace Components (TA Instruments, Inc., 2000).

In this work, we used DSC-TGA model SDT 2960 to decide mass change with temperature in the range 0°C - 800°C under air atmosphere with heating rate of $10^{\circ}\text{C}/\text{min}$. All data were acquired at the Center of Science Technology Equipment, Suranaree University of Technology, Nakhon Ratchasima (CSTE).

The main parts of DSC-TGA used in this thesis work are presented in Figure 2.7.

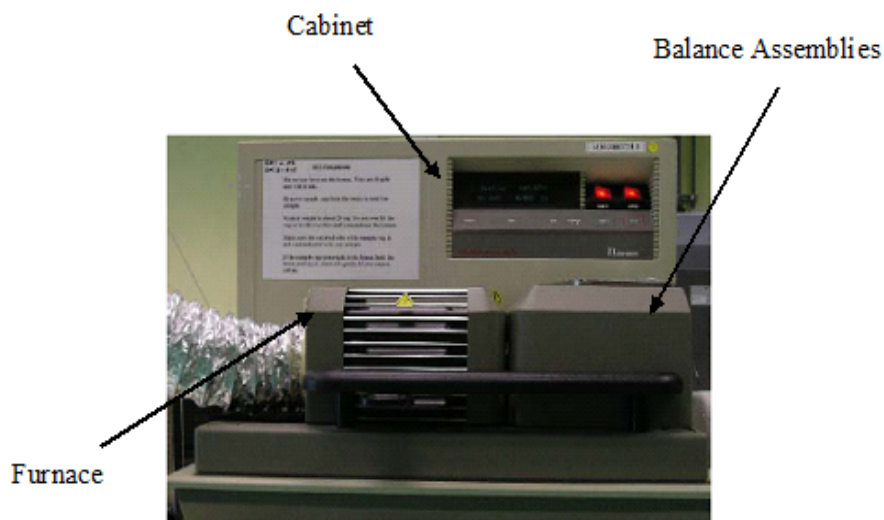


Figure 2.7 The main parts of DSC-TGA (Model SDT 2960): 1) Sample and reference balance assemblies, which provide the precise measurement of heat flow and sample weight. 2) Furnace, which controls the sample atmosphere and temperature and 3) The cabinet, where the system electronics and mechanics are housed.

For TGA experimental set up, we used platinum cups to measure the sample, that it is easy to clean and does not react with most organics and polymers. Tarring the SDT cups certify that the weight measured by the balance reflects the weigh of the sample only. The sample cups should be tarred before each experiment with the furnace closed, the SDT reads the weight of the empty cup and then stores the weigh as an offset, which is material from subsequent weight measurements. For finest exactness, the weight reading must be steady before it is approved as an offset. When using the automatic tare mode, the SDT will define when the weight reading is adequately stable. The result of DSC-TGA is shown in Figure 2.8.

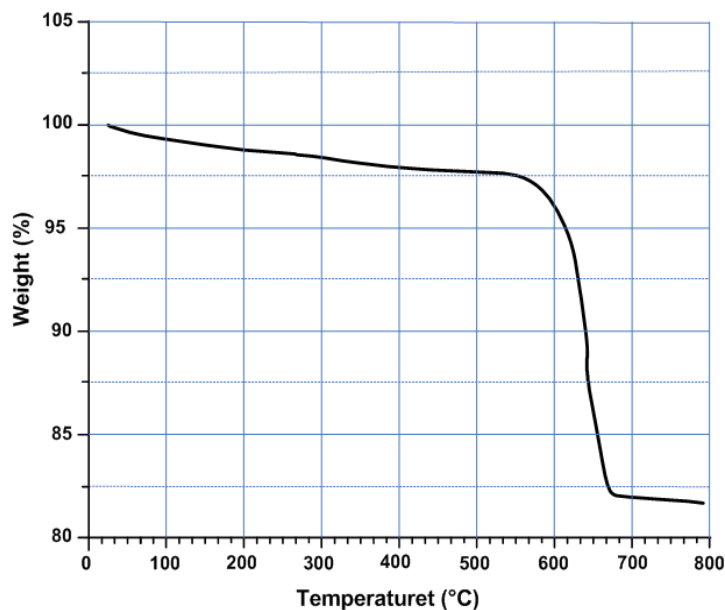


Figure 2.8 DSC and TGA data of ZnS powder.

2.4 Scanning electron microscope (SEM)

The scanning electron microscope or SEM is one type of electron microscope, the image of sample surface is shown by scanning with a high-energy beam of electron in a raster investigate form in high vacuum mode. The electrons interact with atom that make up the sample generate signals that include information about the sample's surface topography, morphology, combination, distribution and other properties. SEM signals included secondary electrons (SE), back-scattered electrons (BSE), characteristic X-rays, cathodoluminescence and transmitted electrons, as shown in Figure 2.9.

There are 4 types of signal to use in SEM:

- 1) Secondary Electrons (SE) is low energy electron (< 50 eV) emitted when primary electrons interact with the surface of the sample. Secondary electrons that are throw out from inner shell (k -orbital) of the specimen atoms by inelastic scattering interactions with beam electrons. SE can generate high topographic

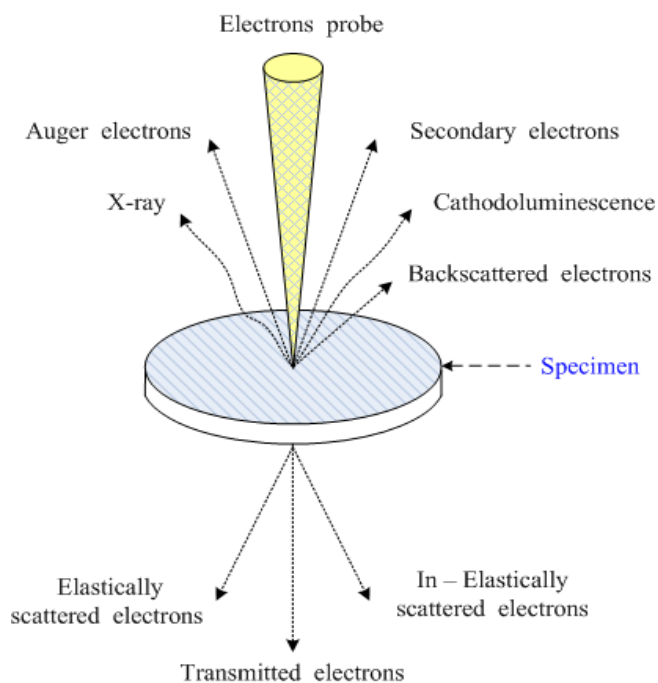


Figure 2.9 Schematic diagram of signals in SEM.

divergence and proposition, show details size less than 1 - 5 nm. The angle of incidence beam of primary electrons to sample surface and surface structure of a sample was depended on the intensity of secondary electrons.

Secondary electron detectors are normal in all SEMs. The signals result from interactions of the electron beam with atoms at the surface of the sample. SEM micrographs have a large deepness of branch yielding property three-dimensional features useful for understanding the surface construction of a sample. Figure 2.10 is a micrograph of S-doped ZnO powder taken from SEM.

2) Back-scattered electrons (BSE) has been reflected from a primary electrons interacted with the sample by elastic scattering interactions. BSE be formed of high-energy electrons activity in the electron beam. The intensity of the back-scattered electrons signal is powerfully associated to the atomic number of the sample, as weighty elements (high atomic number) backscatter electrons more strongly than gentle elements (low atomic number), thus the image appeared

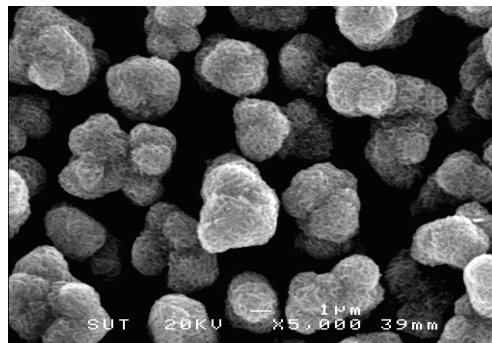


Figure 2.10 SEM micrograph of S-doped ZnO powder.

bright. Back-scattered electrons are used in analytical SEM identical with the spectra made from the characteristic x-rays. BSE are used to detect contrast between areas with different chemical compositions; that the images can recognize about the distribution of different elements in the specimen.

3) Characteristic x-rays are emitted when the electron beam take away from an electron of inner shell from the sample by primary electrons with a higher energy electron to fill the shell and discharge energy. These characteristic x-ray are used to identify the composition and measure the bounty of elements in the sample.

4) Cathodoluminescence, the discharge of light when atoms excited by high-energy electrons come back to their ground situation, is similar to UV-induced fluorescence, and some materials and some fluorescent stain, show both phenomena.

In this thesis, the surface morphology of the S-doped ZnO samples was observed on a JEOL JSM-6400 scanning electron microscope. All data were acquired at the Center of Science Technology Equipment (CSTE), Suranaree University of Technology.

The main parts of SEM are:

- 1) Electron Gun
- 2) Condenser Lens

- 3) Scan coil
- 4) Objective Lens
- 5) Detector

The principles schematic diagram of scanning electron microscope as shown in Figure 2.11

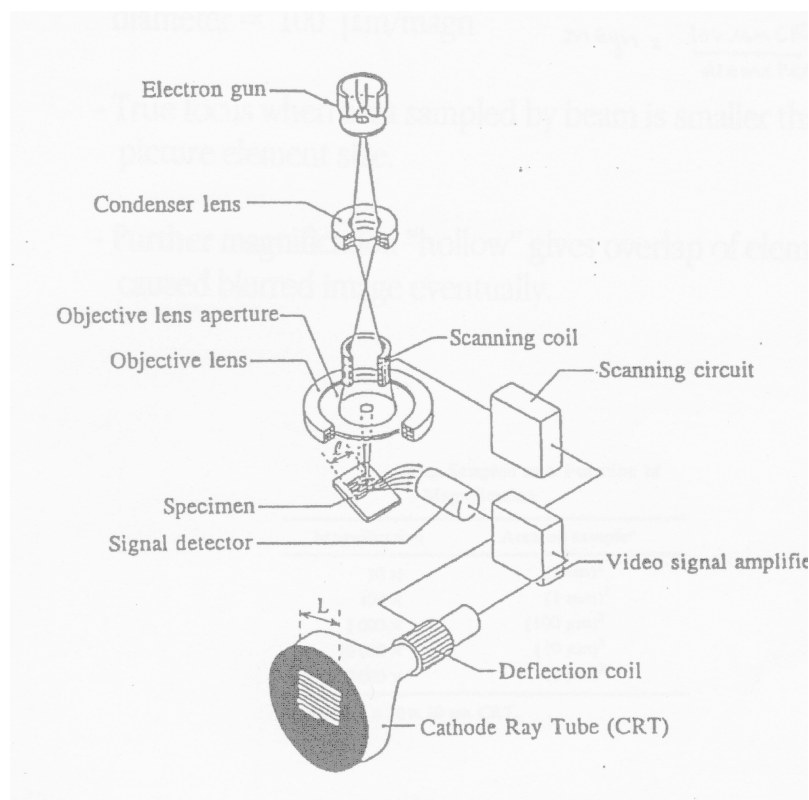


Figure 2.11 Principles schematic illustration of SEM (JEOL, Ltd., 1989).

In SEM techniques, an electron beam is emitted from an electron gun provided with a tungsten filament cathode. Tungsten is generally used in thermal electron guns because it has the highest melting point and lowest vapour pressure of all metals, whereby permitting it to be heated for electron emission. The electron beam is focused by two condenser lenses. The beam passes through pairs of scanning coils in the electron column, regularly in the final lens, which deflect the beam in the x and y axes so that it scans in a raster create over a square area of

the sample surface.

In SEM observation, the electron beam generated from the electron gun that is finely focused and illuminated on the specimen by electron lenses and interacts with the specimen, as the beam is scanned over the specimen surface in both x- and y-directions, the electron lose energy by repeated random scattering and absorption. The secondary electrons and backscattered electrons are detected by particular detectors. The beam current absorbed by the specimen can also be detected and used to create images of the distribution of specimen current. The raster is scanning of the CRT display is synchronized with that of the beam on the specimen in the microscope, and the resulting image is therefore a distribution map of the intensity of the signal being emitted from the scanned area of the specimen. By amplifying these electron signals and modulating their brightness on the observation CRT, a specimen image is displayed on the CRT.

Energy dispersive x-ray spectroscopy (EDS) is an x-ray analysis based on electronic transition between inner atomic shells. EDS in scanning electron microscope technique gives information on the elemental composition. Primary electrons knock out electrons from a shell of low energy. An electron from a higher shell subsequently fills the vacancy, emitting radiation of energy in the form of x-ray fluorescence. The emitted x-ray produces a charge pulse in a semiconductor detector. Current is converted into a voltage pulse, then into a digital signal. The signal adds a count to the appropriate channel of a multi-channel analyzer (MCA).

The main parts of EDS are:

- 1) Electron source
- 2) Detector
- 3) Electronic components
- 4) Analyzer

The basic parts of EDS are shown in Figure 2.12.

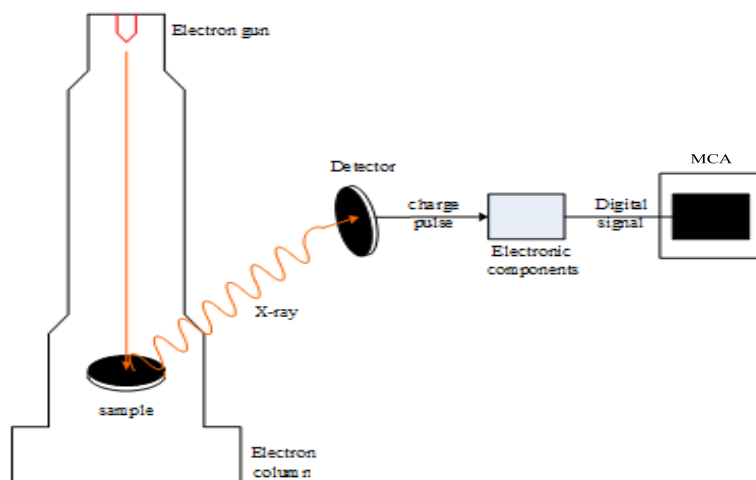


Figure 2.12 Schematic diagram of an EDS.

EDS can be used to identify the type of element composing the sample. The detection limit in bulk materials is about 0.1 wt%. This testifies to the fact that the EDS are embodying many advanced features of semiconductor technology. It is compact, stable, robust, easy to use, inexpensive, can quickly interpret the readout, and quantitative for some samples (flat, polished, homogeneous).

2.5 Transmission electron microscope (TEM)

Transmission electron microscopy (TEM) is a microscopy technique by which an electron beam is transmitted through an ultra thin specimen, interacting with the specimen and a beam which has passed the specimen. An image is formed from the interaction of the electrons transmitted through the specimen and scattered is observed after being magnified by electron lenses; the image is magnified and focused onto an imaging device, such as a fluorescent screen, on a layer of photographic film, or to be detected by a sensor such as a CCD camera. TEM has the ability of imaging at a significantly higher resolution than light

microscopes, owing to the small de Broglie wavelength of electrons.

Theoretically, d is the maximum resolution, that one can obtain with a light microscope has been limited by the wavelength of the photons that are being used to probe the sample (λ) and NA is the numerical aperture of the system,

$$d = \frac{\lambda}{2n \sin \alpha} \approx \frac{\lambda}{2NA}. \quad (2.12)$$

Electrons have both wave and particle properties and their wave-like properties mean that a beam of electrons can be made to behave like a beam of electromagnetic radiation. The wavelength of electrons is found by equating the de Broglie's equation to the kinetic energy of an electron:

$$\lambda_c = \frac{h}{\sqrt{2m_0E \left(1 + \frac{E}{2m_0c^2}\right)}}, \quad (2.13)$$

where, h is Planck's constant, m_0 is the rest mass of an electron and E is the energy of the accelerated electron. An additional correction must be made to account for relativistic effects, as in TEM an electron's velocity approaches the speed of light, c .

Electrons are normally generated in an electron microscope by a process known as thermionic emission from a filament, usually tungsten, in the same manner as a light bulb, or alternatively by field electron emission. The electrons are then accelerated by an electric potential and focused by electrostatic and electromagnetic lenses onto the sample. The transmitted beam includes information about electron density, phase and periodicity; this beam is used to form an image.

TEM is composed of several components, which include a vacuum system in which the electrons travel, an electron emission source for generation of the

electron stream, a series of electromagnetic lenses, as well as electrostatic plates. The layout of optical components in basic TEM was shown in Figure 2.13.

At the top of the TEM column is the electron gun, which is the source of electrons. The electrons are accelerated to high energies (typically 100 - 400 keV) and then focused towards the sample by a set of condenser lenses and apertures. The source is chosen so that the rates of electrons incident on the sample per unit area and leaving the source per unit solid angle are maximized. This is so that the maximum amount of information can be extracted from each feature of the sample.

Typically a TEM consists of three stages of lenses. The stages are the condenser lenses, the objective lenses, and the projector lenses. The condenser lenses are responsible for primary beam formation, while the objective lenses focus the beam down onto the sample. The projector lenses are used to expand the beam onto the phosphor screen or other imaging device. The magnification of the TEM is due to the ratio of distances between the specimen and the objective lens image plane. Additional quad or hexapole lenses allow for the correction of asymmetrical beam distortions.

Crystal structure can also be investigated by High Resolution Transmission Electron Microscopy (HRTEM), also known as phase contrast. When utilizing a field emission source, of uniform thickness, the images are formed due to differences in phase of electron waves, which is caused by specimen interaction. Image formation is given by the complex modulus of the incoming electron beam.

In the central section of the microscope the electron beam interacts with the specimen, and the resulting electron are gathered and focused ready for further magnification of the desired images. As the electrons are incident on the sample they may be scattered by several mechanisms.

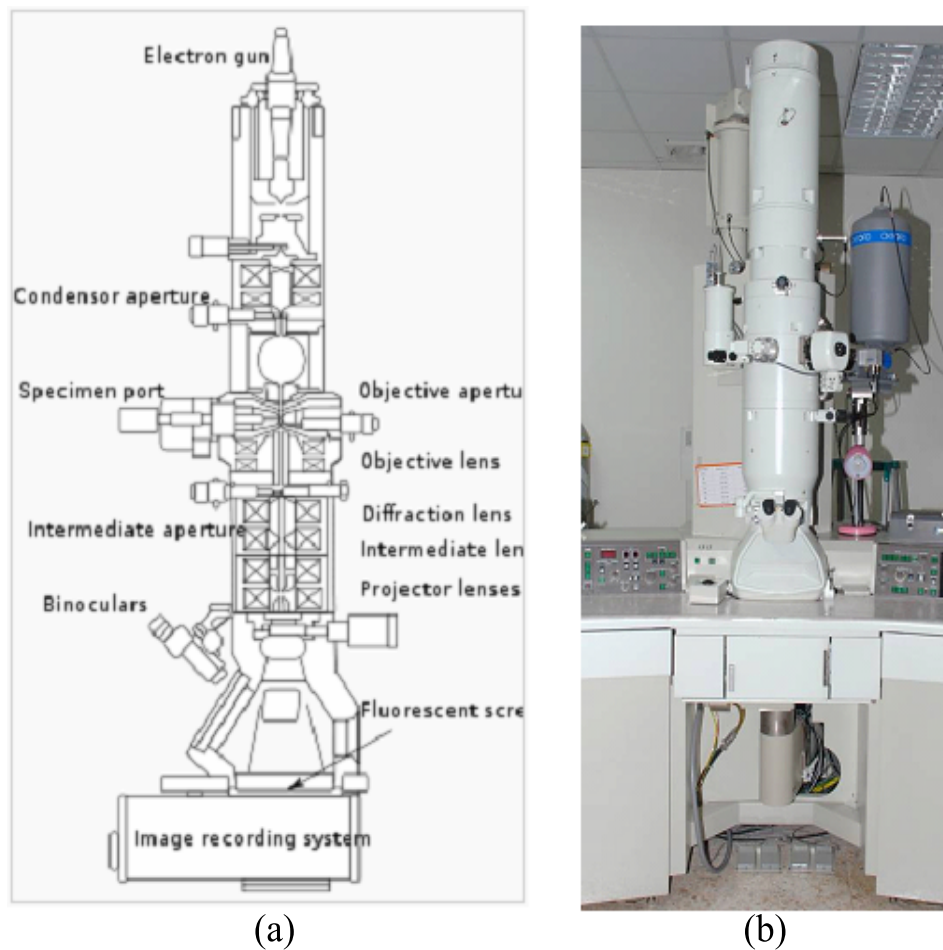


Figure 2.13 (a) Cross section of column in TEM (JEOL, Ltd., 1996) and (b) Transmission electron microscopy JEOL JEM-2010.

These scattering mechanisms will change the angle the electrons are moving at relative to the optic axis, and may be elastic or inelastic. It is by measuring the changes to the electrons on passing through the sample, either by measuring the angle that they have been scattered through or by measuring the amount of energy that they have lost, that we can gather information about the sample. The specimen itself is inserted into the path of the electrons, and for the best resolution must be extremely thin; a few nanometers. Once inside the microscope, the specimen sits right inside the objective lens and therefore be small, typically less than 3 mm in diameter. It is necessary to align the specimen very accurately

with the electron beam to achieve the required images. Common specimen holders allow rotation about two horizontal axes, along with lateral movement. Other holders might include heating elements or nano-indenters to deform the specimen as it is imaged.

Electron diffraction (ED) is the one of important diffraction techniques of three groups, X-ray diffraction, Neutron diffraction, and electron diffraction. Diffraction in transmission electron microscopy used technique to call "Selected Area Electron Diffraction, SEAD", which typically has an energy ranging from 100 - 400 keV.

Electron diffraction in TEM resulted from interactions of the electron beam with planes of specimen and produced small angles. An electron of diffraction from planes of atom in specimen will be focused by objective lens at diffraction points. Electron diffraction can be identified by Bragg's equation in equation (2.1).

Selected area diffraction pattern can be generated by adjusting the magnetic lenses such that the back focal plane of the lens rather than the imaging plane is placed on the imaging apparatus. For thin crystalline samples, this produces an image that consists of a pattern of dots in the case of a single crystal, or a series of rings in the case of a polycrystalline or amorphous solid material. For the single crystal case the diffraction pattern is dependent upon the orientation of the specimen and the structure of the sample illuminated by the electron beam. This image provides the investigator with information about the space group symmetries in the crystal and the crystal's orientation to the beam path. This is typically done without utilizing any information but the position at which the diffraction spots appear and the observed image symmetries.

The information images in a TEM technique is a give result of two characters:

1) Image: show details of the microstructure, which magnification ranges 10000X to 1000000 X.

2) Diffraction pattern: information about atomic positions within the material.

Figure 2.14 shows ray diagrams in both images. From the image we can widely interpret data, such as the structural defects. Data from TEM image in both diffraction pattern and image will be show position and characteristic of deficiency in specimen.

The image of electron diffraction in TEM techniques will be had two conceptions such as

1. Diffraction angle (2θ) is small angle only 3 - 4 theta as shown in Figure 2.15.

2. Selected area diffraction was found Ewald sphere, which sphere cuts through the reciprocal lattice point, the Bragg condition is satisfied. Diffraction patterns will be formed at the intersections as presented in Figure 2.16.

Consider Figure 2.15 and Figure 2.16; these figures show geometry of electron diffraction with reciprocal space lattice. A perfectly aligned crystal shooting down the reciprocal space lattice planes axis. Only spots lying on the Ewald sphere are diffracting. Perfectly aligned external gives circular diffraction rings from intersection of planes with a circle. By the way, from Bragg's equation (2.1), when $n = 1$ for the first diffraction spot and θ is small. We can use small angle approximation

$$\sin \theta \sim (R/2) \times 1/L = R/2L \quad (2.14)$$

$$d \frac{R}{L} = \lambda \quad (2.15)$$

$$d = \lambda L/R \quad (2.16)$$

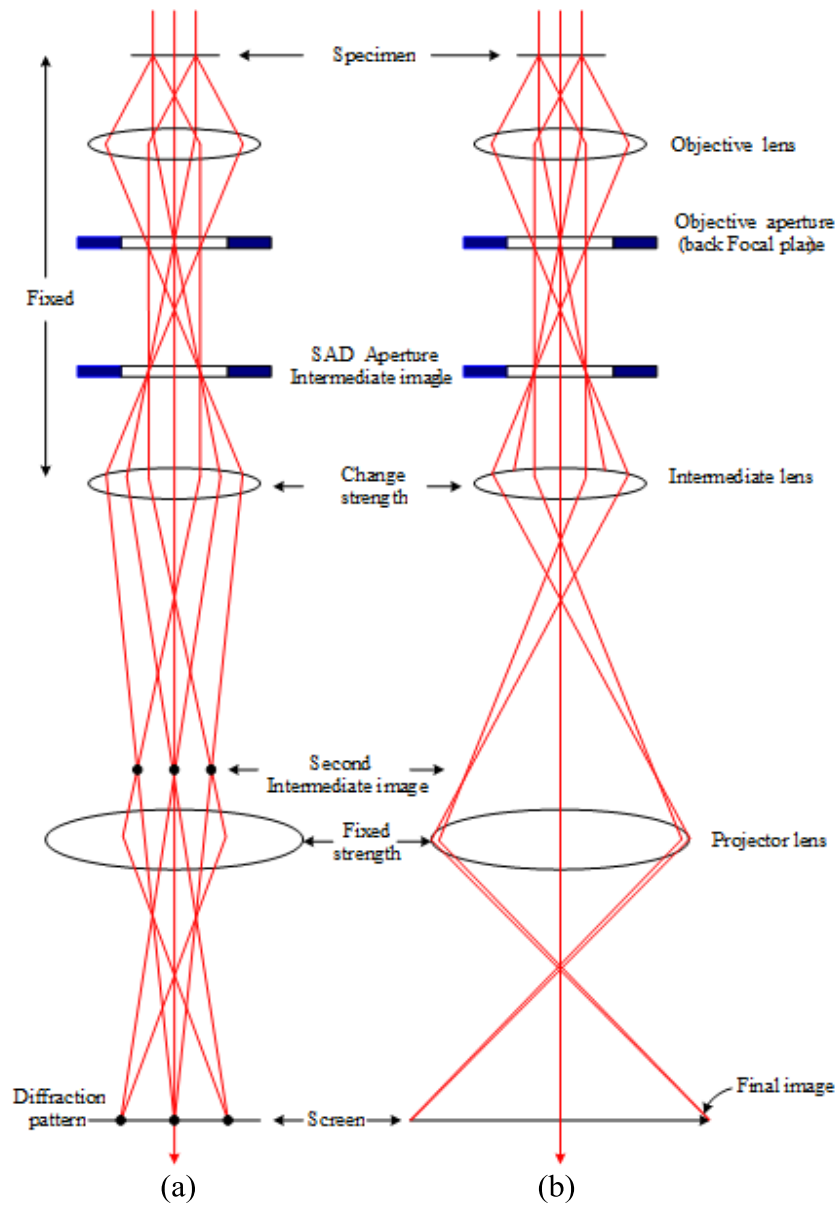


Figure 2.14 Ray diagrams of (a) diffraction pattern and (b) image [adapted from (William and Carter, 1996)].

or

$$\lambda L = Rd \quad (2.17)$$

where λ is the wavelength of the TEM accelerating voltage (nm), L is the camera length (mm), d_{hkl} is the lattice spacing (nm), R is the measured distance between

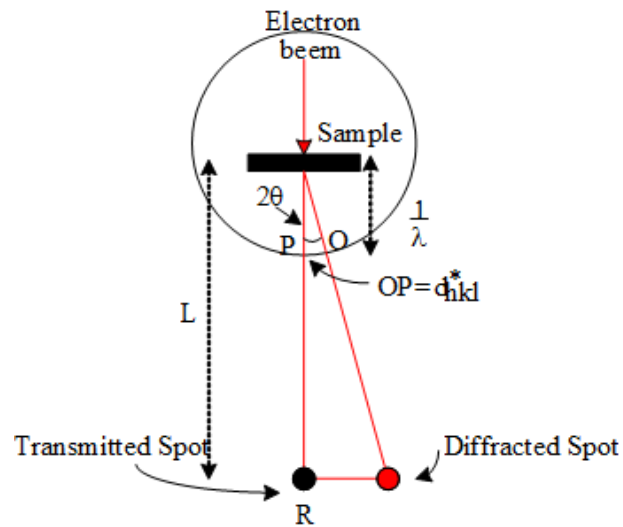


Figure 2.15 Graphical representation of geometry of Bragg's Law [adapted from (Hammond, 1992)].

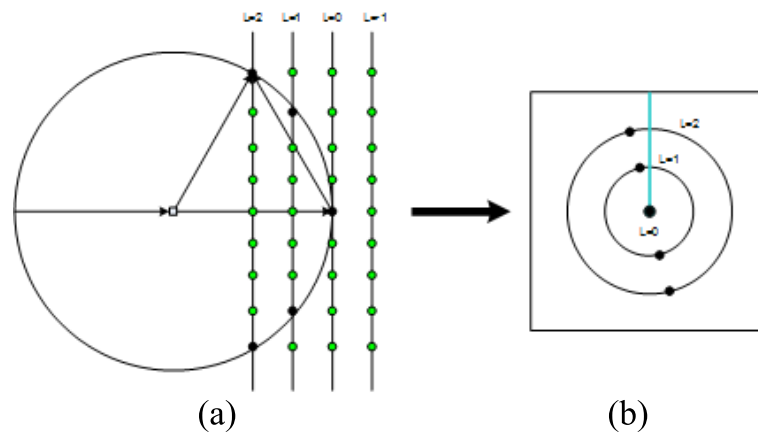


Figure 2.16 Creation of diffraction pattern (a) reciprocal space lattice planes and (b) detector face on view [adapted from (Hammond, 1992)].

two adjacent diffraction spots on a single crystal diffraction pattern or half the diameters on a polycrystalline diffraction pattern (mm)

The product λL is called the Camera Constant. However, this value is not a constant, it follows with accelerating voltage or electron energy. The camera constant calibration is the most common calibration used in electron diffraction. It allows the user to identify the crystal lattice spacing of material being ob-

served, which helps to identify the material. This identification is accomplished by measuring distances between spots on a single crystal diffraction pattern, or ring diameters on polycrystalline diffraction pattern.

2.6 X-ray absorption spectroscopy (XAS)

X-ray absorption Spectroscopy (XAS) is a powerful technique to investigate the electronic structure of materials, chemical state, oxidation state coordination number, and used to study local structure. The measurement data is usually collected at the Synchrotron laboratory, where the oscillations observed on the higher energy side of an absorption edge, these oscillations arise as a result of interference effects between the outgoing photoelectron wave and the backscattered wave; caused by the reflection of incident photoelectron wave by neighbouring atoms.

X-ray absorption spectroscopy measures the x-ray absorption $\mu(E)$ as a function of x-ray energy,

$$E = \hbar\omega. \quad (2.18)$$

The x-ray absorption coefficient is determined from the decay in the x-ray intensity I with distance x . In the experiment, we will obtain the x-ray absorption coefficient in the term of thickness independent,

$$I = I_0 e^{-\mu x}, \quad (2.19)$$

where I_0 is the intensity of the incoming x-ray beam, I is the intensity of the beam after pass through the sample, and x is the thickness of the sample, μ is the

definition of absorption coefficient, as shown in Figure 2.17.

The absorption edge corresponds to an x-ray photon having enough energy to just free a bound electron in the atom. When the electron are in the most tightly bound $n = 1$ shell the edge is called the K -edge. For the next most tightly bound is $n = 2$ shell, the corresponding edge are called the L -edge. At present these edges are the only ones used to observe XAS, though in principle $n = 3$ or higher shells could be used.

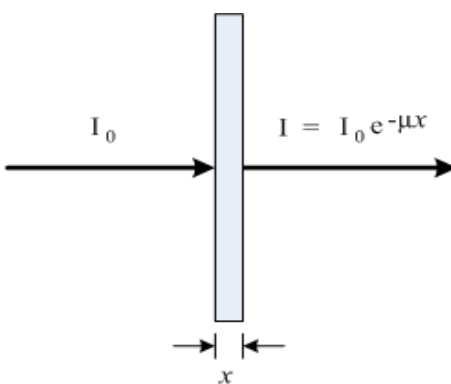


Figure 2.17 Schematic view of x-ray absorption measurement in transmission mode.

In the process of absorption, electrons in shells: K , L or M shell will be excited by photoelectron absorption where the photon is completely absorbed, and leaving behind a core hole in the atom. The excited atom with its core hole has some probability of having additional excitations. The core hole, empty state, will be created in the inner shell, and the energy level of the shell is used to define the type of absorption edge as show in Figure 2.18.

The x-ray spectrum is generally divided into two regions (1) the x-ray absorption near edge structure (XANES) which extends up to 40 - 50 eV and (2) the extended x-ray absorption fine structure (EXAFS) typically extending to 1000 eV above the absorption edge as shown in Figure 2.19.

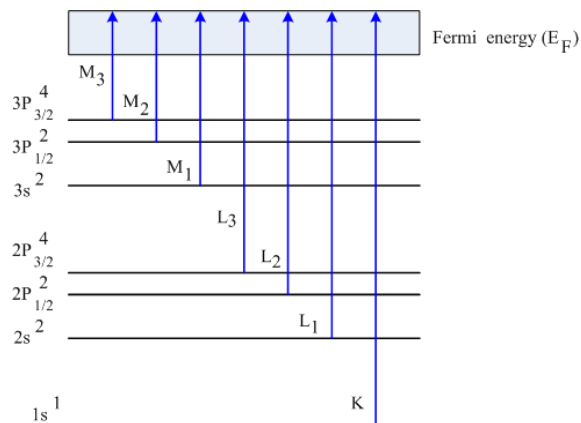


Figure 2.18 The relationship between the energy transitions and absorption edges [adapted from (Rehr and Albers, 2000)].

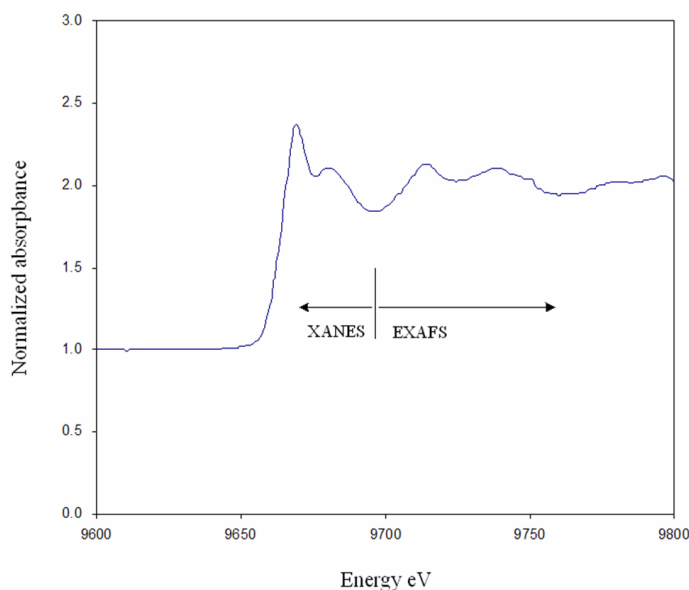


Figure 2.19 Normalized Zn K-edge absorption spectra classified into two regions, XANES and EXAFS.

2.6.1 X-ray absorption near-edge structure (XANES)

X-ray absorption near edge structure, or XANES provide information on the valence state, electronic structure and coordination geometry of the absorbing atom. XANES structure in an absorption spectrum cover the range between the threshold and the point at which the extended x-ray absorption fine structure

(EXAFS) being. XANES extending to an energy of the order to 40 - 50 eV above the edge.

This region is the signal of x-ray absorption caused by migration status of the electron energy from valence state to the continuum state. XANES structure is associated with the atomic energy structure and energy density of the state space systems, that XANES are definite to the chemical environment of atom, which use to chemical analysis of fingerprinting and principle component analysis. Therefore, XANES is usually used to study the oxidation state and the local orientation of material.

XANES structure is participated of scattering signal of low energy of photoelectron, and the majority is will be multiple scattering. We can calculate wavelength of photoelectron (λ_c) from wave number (k) by equation,

$$k = 2\pi/\lambda_c. \quad (2.20)$$

Wave number of photoelectron will be change with the energy of x-ray photo energy (E), that can be described by

$$k = \sqrt{2m(E - E_0)/\hbar^2}, \quad (2.21)$$

where E_0 is the threshold energy or ionization energy.

The absorption coefficient in equation (2.19) can be derived from the transition rate given by Fermi's Golden Rule, described by

$$\tilde{\mu}(E) \propto \sum_f |\langle f | \hat{\varepsilon} \cdot \vec{r} | i \rangle|^2 \delta(E_i - E_f + \hbar\omega), \quad (2.22)$$

where $|i\rangle$ is the initial core *ket* state vector, $\langle f|$ is the final *bra* state vector of

the excited electron, E is the energy of absorbed x-ray photon, E_i is the energy of initial state, E_f is the energy of final state, $\hbar\omega$ is the energy of x-ray photon energy, $\hat{\epsilon}$ is the x-ray polarization vector and $\tilde{\mu}(E)$ is absorption coefficient with ignoring of core hole life time and experimental resolution (Ankudinov et al., 1998).

2.6.2 Extended x-ray absorption fine structure (EXAFS)

EXAFS gives information about the number, nature and interatomic distances of the neighbours from the absorption atom. The extended x-ray absorption fine structure is a consequence of the modification of the photoelectron final state due to scattering by the surrounding atoms. The absorption fine structure starting from electron atom scattering phase shifts. The electron scattering is treated using a spherical wave augmentation which takes into account the finite size of the atoms. Multiple scattering effects are included by classifying multiple scattering paths by the total path lengths. The effects are quite large but appear to make quantitative but not qualitative change on the single scattering contribution. The final state photoelectron is modified to first order by a single scattering from each surrounding atom. Quantum mechanically the photoelectron must be treated as a wave emitted from the absorber with wavelength λ is given by the de Broglie relation

$$\lambda = \frac{h}{p}, \quad (2.23)$$

where p is the momentum of the photoelectron and h is Planck's constant. In EXAFS regime p can be determined by the free electron relation

$$\frac{p^2}{2m} = h\nu - E_0, \quad (2.24)$$

where $h\nu$ is the energy of frequency ν photon, E_0 is the bonding energy of the photoelectron and m is mass of the excited electron.

For a separated atom the photoelectron can be illustrated as an outgoing wave as shown in Figure 2.20 by the solid line of Zn atom. The surrounding atoms will scatter the outgoing wave as indicated by the dashed lines of S atoms. The final state is the superposition of the outgoing and scattered waves. The backscattered waves in Figure 2.20 will add or take off from the outgoing wave at the center depending on their associate phase. The total amplitude of the electron wave function would be improved or decreased, respectively, thus changing the possibility of absorption of the x-ray correspondingly. The phase varies with the wavelength of the photoelectron depends on the distance between the center atom and backscattering atom. The deviation of the backscattering strength as a function of energy of the photoelectron depends on the type of atom doing the backscattering. Thus EXAFS contains information on the atomic surroundings of the center atom.

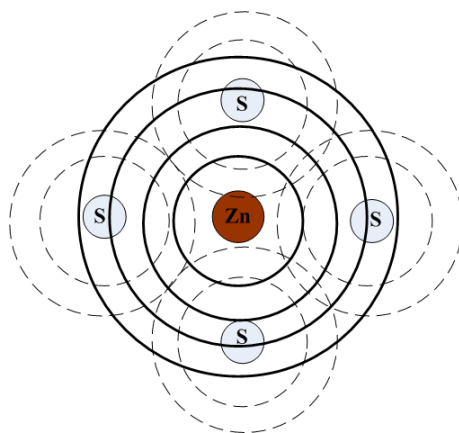


Figure 2.20 Schematic of the radial portion of the photoelectron wave.

The oscillation of x-ray absorption will be show of the absorption edge,

EXAFS function can be expressed by

$$\chi(E) = \frac{[\mu(E) - \mu_0(E)]}{\Delta\mu_0}, \quad (2.25)$$

, (2.25) where $\nu(E)$ is the x-ray absorption coefficient, $\nu_0(E)$ is smooth atomic background absorption coefficient.

Furthermore, in the EXAFS analysis $\chi(E)$ could be converted from E space to k space by the relations $k = \sqrt{2m(E - E_0)/\hbar^2}$. Then the function can be transformed from $\chi(E)$ to $\chi(k)$ for general purpose. In theoretical procedure, the $\chi(k)$ can be described by (Wilson et al., 2000).

$$(2.26)$$

$$\chi(k) = \sum_j \frac{S_0^2 N_j}{k R_j^2} |f_j(k, \pi)| \sin [skR_j + \phi_j(k)] e^{-2\sigma_j^2 k^2} e^{-2R_j/\lambda(k)}, \quad (2.27)$$

, (2.26) where N_j is the number of neighbour in j shell of surrounding atoms, k is photoelectron wave vector, f_j is the scattering amplitude, $S_0^2(k)$ is the amplitude reduction term due to many-body effect, R_j is radial distance from absorbing atom to j shell, $\lambda(k)$ is electron mean free path, σ_j is the Debye-Waller factor and $\phi(k)$ accounts for the total phase shift of the curve wave scattering amplitude along the scattering trajectory.

The length between core atom and backscattering atoms or the path-length change the phase differing with the wavelength of photoelectron. In addition, different types of encompassing atoms vary the backscattering depth as a function of photoelectron energy. It is accepted that, by the careful analysis of the EXAFS structure, one can receive significance structural parameters surrounding the center atom.

2.7 X-ray absorption spectroscopy experimental set up

The x-ray absorption spectroscopy experiment is usually carry out at a synchrotron radiation source, because of high intensity and energy adaptable capability of generated x-ray photon, and the capability to obtain the continuous absorption spectrum over broad energy range. In generally, there are three types of x-ray absorption measurements: transmission-mode XAS, fluorescence-mode XAS and electron-yield XAS as schematic illustration shown in Figure 2.21.

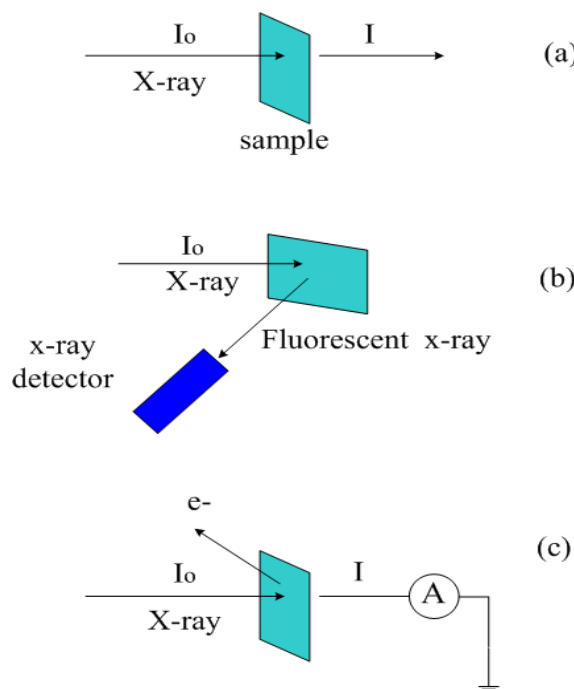


Figure 2.21 The three modes of XAS measurement (a) transmission mode, (b) fluorescence mode and (c) electron yield. [adapted from (Kawai, 2000)].

In the transmission-mode, after the energy of x-ray photons being altered by x-ray double crystals monochromator, the intensities of incident x-ray photon beam (I_0) and the transmitted x-ray photon beam (I) were measured by ionization chambers as shown in Figure 2.22. We will obtain the x-ray absorption coefficient in the term of thickness independent based on equation (2.19). The experimental set up of XAS experimental station at XAS beam line, Siam Photon Laboratory,

SLRI is shown in Figure 2.23.

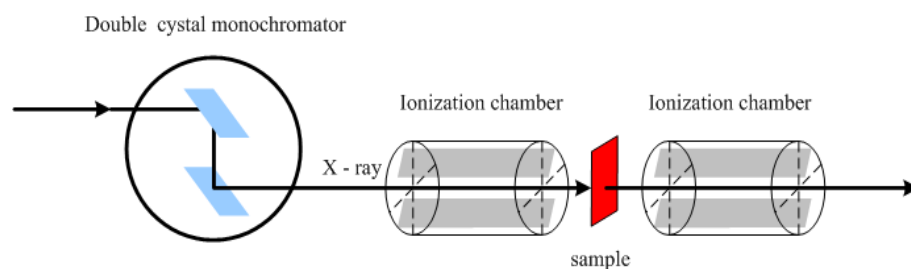


Figure 2.22 .Schematic illustration of the experimental setup of transmission-mode X-ray absorption spectroscopy

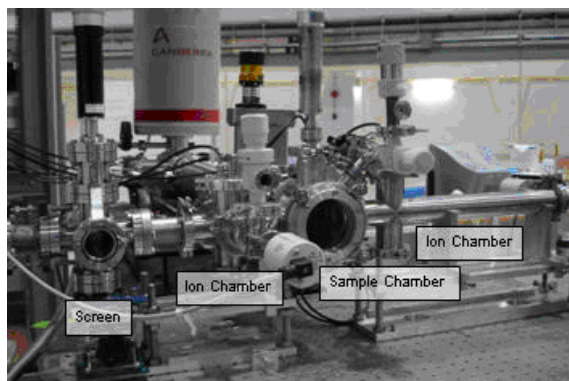


Figure 2.23 .XAS experimental set up at the Siam Photon Laboratory, Synchrotron Light Research Institute

In the part of the transmission mode, the fluorescence mode and the electron yield are also ability for the measurement of the absorption coefficient. In the x-ray absorption phenomena, where the electrons knock out an electron from a shell of low energy an electron from a higher energy level fill the vacancy and emitting radiation of energy, the emitted energy x-ray photon will be liberated as explained in Figure 2.24 (a) and the fluorescence x-ray can be find out. Moreover, de-excitation can cause the Auger effect, where the electron decrease to lower energy state, a second electron can be excited to the continuum state and maybe go out from the sample as shown in Figure 2.24 (b), and the electron-yield XAS detectors can be detected. However, both modes are instantly equivalent to the absorption

ability of the sample. Hence, the three techniques are alterable for the study of the structure of material using the absorption ability of the sample.

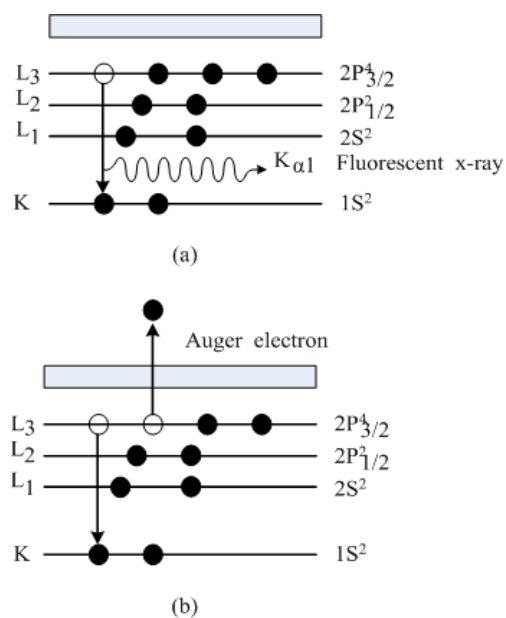


Figure 2.24 The excited state (a) x-ray fluorescence and (b) the Auger effect. [adapted from (Koningsberger and Prins, 1998)].

CHAPTER III

STANDARD CHARACTERIZATION

RESULTS AND DISCUSSION

In this chapter, the structural characterization and the interpretation of the experimental data will be presented and discussed. First, the preparation of sulfur doped ZnO powder by oxidative annealing is presented. Then characterization results by x-ray diffraction (XRD), thermal gravimetric analysis (TGA), scanning electron microscope (SEM), transmission electron microscope (TEM) images and electron diffraction will be given and discussed. The x-ray absorption spectroscopy (XAS) data in both EXAFS and XANES regions, will be analyzed and presented with discussion in chapter IV.

3.1 Oxidative annealing

ZnO nanocrystals have been synthesized by various techniques. In this work, the synthesis of ZnO:S nanocrystals powder was based on thermal oxidation method called oxidative annealing (Smith et al., 2007). This technique involves neither tiresome catalytic process nor carrying aqueous thermal decomposition. Indeed, the synthesis process was carried out in a normal oven. The starting source material was pure ZnS powder.

S-doped ZnO powder was prepared by oxidative annealing of ZnS powder in normal atmosphere. First, we annealed ZnS in air at 200°C, 300°C, 400°C, 500°C, 600°C, 700°C and 800°C for 2 hour at each temperatures, the powder could be

oxidized and results in new product. After that, the samples were cooled down in air. Then the annealing products at each temperature were dried. Finally, the products were kept in a humidity controlled cabinet at room temperature before characterizations.

A NIKON stereomicroscope model SMZ-U with magnification 10X was used to study the physical appearance of the powder of sample. Figure 3.1 shows the pictures of ZnS powder and the annealing products.

The products formed in the temperature range of 200°C to 300°C appear to be white color. The colors of the products begin to become light-yellow at products formed in the temperature range of 200°C to 300°C. At 400°C to 600°C, the colors gradually appear become more yellow (the color of sulfur). After that, the yellow color starts to disappear and became white powder again at 800°C. This suggests some chemical reaction of the starting material has occurred during the annealing. Next, the structure of the products will be characterized by XRD, TGA, SEM, TEM, EDS and XAS.

3.2 X-ray diffraction (XRD)

The BRUKER X-ray diffractometer model D 5005, wave length 1.54 Å was used to study the structure of the ZnO:S nanocrystals obtained. The patterns of XRD for ZnS powder and annealing products prepared at different annealing temperatures (200°C, 300°C, 400°C, 500°C, 600°C, 700°C and 800°C) are shown in Figure 3.2

From Figure 3.2, it can be seen that the annealing products at temperature 500 C and lower still posses the ZnS structure. The structural transformation can be seen at temperature 600°C. At 600°C - 800°C, the XRD pattern shows that the products are almost pure ZnO. We concluded that the zincblend ZnS powder

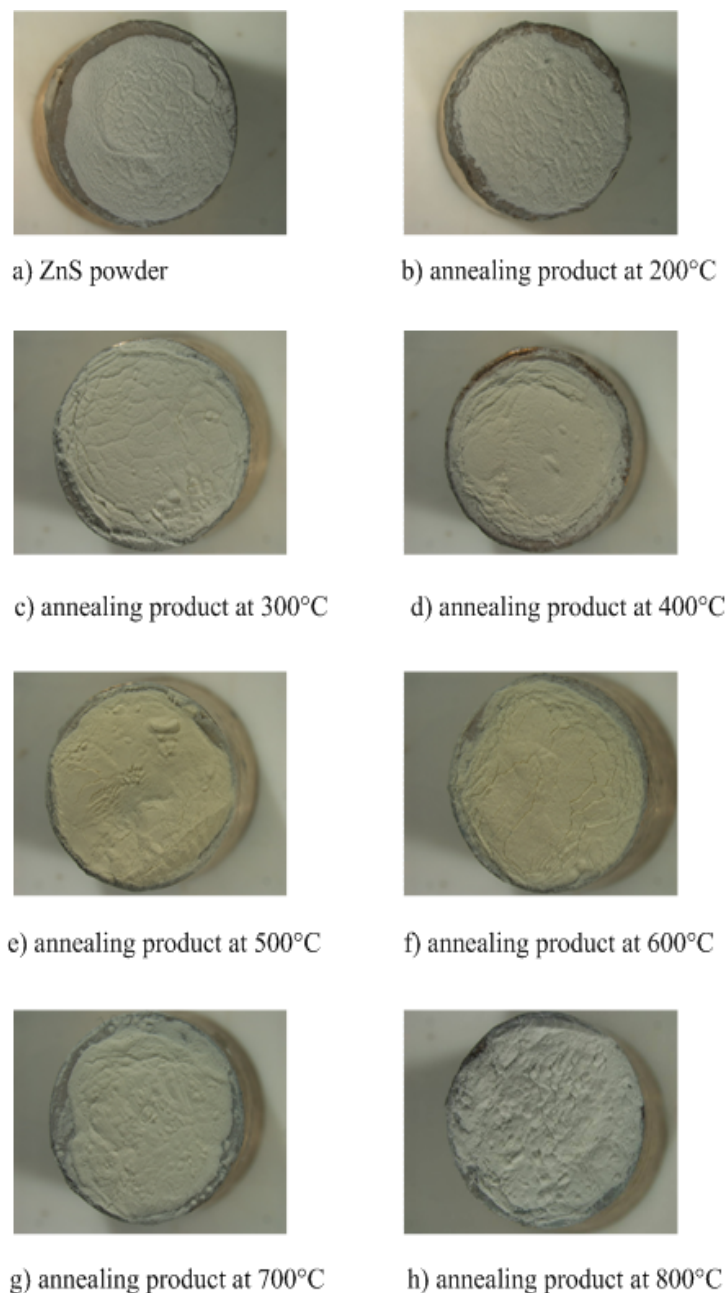


Figure 3.1 ZnS powder and ZnO:S annealing products.

can be transformed to wurtzite structure of ZnO at annealing temperature 600°C and above.

From full-width at half-maximum (FWHM) of the strongest diffraction peak at each temperature, the mean crystal grain size was determined by Debye-Scherrer formula using equation 2.2. The obtained particle sizes are shown in Table 3.1.

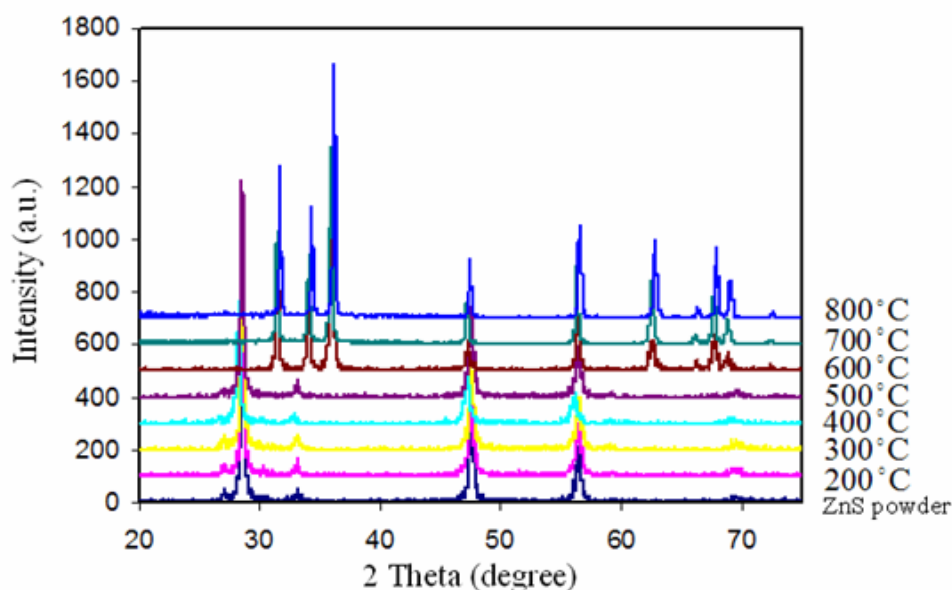


Figure 3.2 XRD patterns of ZnS and annealing products.

Table 3.1 The mean crystal grain size of ZnS powder and ZnO:S annealing products at 200°C - 800°C calculated from Debye-Scherrer formula.

Sample	A	B	C	D	E	F	G	H
annealing temperature (°C)	RT	200	300	400	500	600	700	800
Particle diameter (nm)	51.91	53.30	53.65	61.57	57.05	55.80	55.58	72.45

The grain sizes of ZnS and ZnO:S products are about 50 - 70 nm which can be said that the products are nanocrystals. These results are confirmed by the measurement using TEM. Noting that, the discrepancies of particle size measurement may arise from fact that the diffraction angle in the x-ray diffractometer model D 5005 used in this work was not well calibrated and the instrumental broadening was not taken into account. The diffraction angles were also shifted

due to some misalignment.

The Miller's index numbers ($h k l$) are assigned to the corresponding diffraction peaks as shown in Figure 3.3 (group I) and Figure 3.4 (group II), respectively.

The lattice parameters calculations are summarized in Table 3.2 - 3.5.

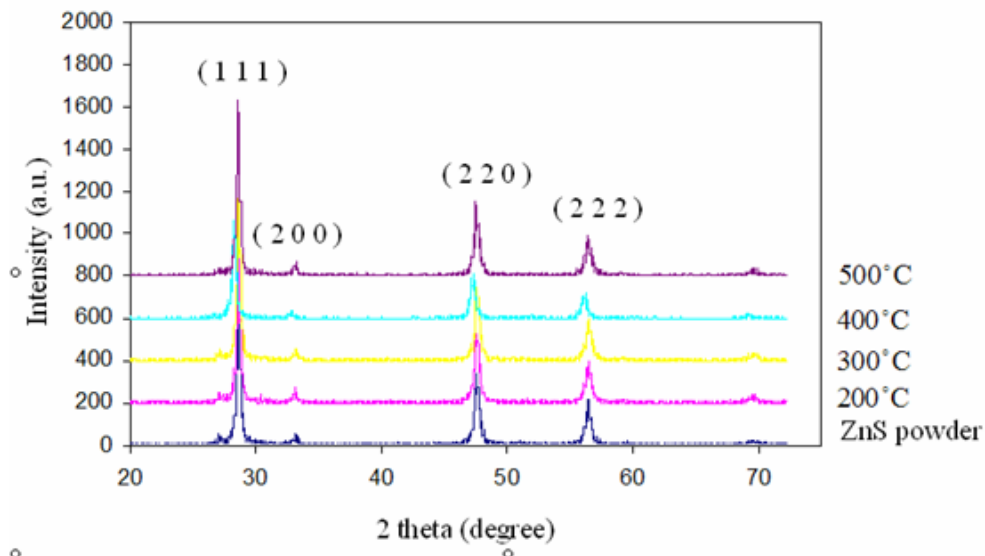


Figure 3.3 XRD patterns of ZnS powder and annealing products from 200°C - 500°C.

Table 3.2 The assigned ($h k l$) indices for group I (ZnS) $2d_{hkl} \sin \theta = n\lambda$ and $d_{hkl} = \frac{a}{\sqrt{h^2+k^2+l^2}}$.

Peak No.	2θ	$\sin^2 \theta$	$1 \times \frac{2 \sin^2 \theta}{2 \sin^2 \theta_{min}}$	$3 \times \frac{2 \sin^2 \theta}{2 \sin^2 \theta_{min}}$	$h^2 + k^2 + l^2$	($h k l$)
1	28.56°	0.0608	1.0000	3.0000	3	(111)
2	33.09°	0.0811	1.3329	3.9986	4	(200)
3	47.52°	0.1623	2.6681	8.0044	8	(220)
4	56.29°	0.2225	3.6571	10.9714	11	(222)

From Tables 3.2 - 3.5 the lattice parameter for the annealed products at 200°C - 500°C (ZnS) is obtained to be $a = 5.41 \text{ \AA}$. The lattice parameters for the

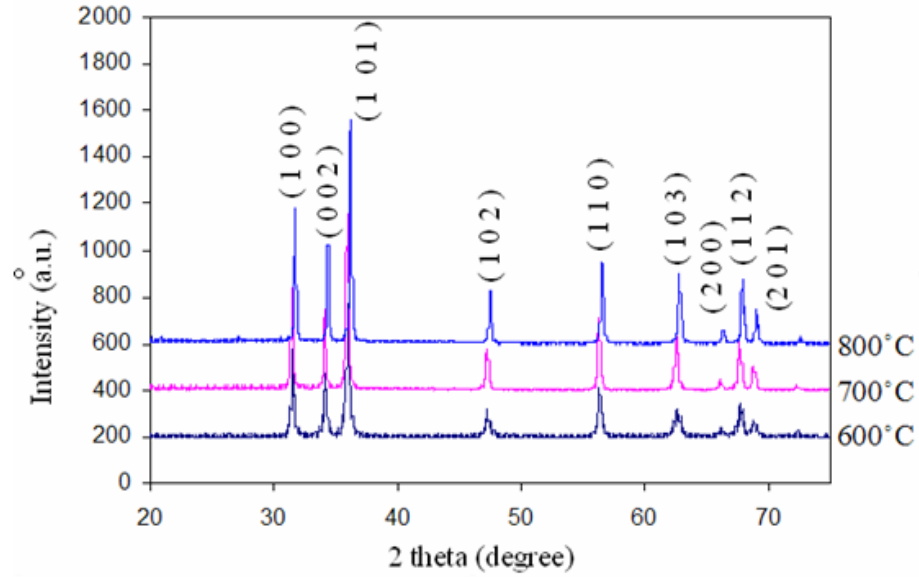


Figure 3.4 XRD patterns of ZnO:S annealing products at 600°C - 800°C.

Table 3.3 Calculation of lattice parameter for the XRD peaks group I (ZnS).

Peak No.	(h k l)	2θ	θ	$a_{hkl} = \frac{n\lambda\sqrt{h^2+k^2+l^2}}{2\sin\theta}$ (Å)
1	(111)	28.56°	14.29°	5.409
2	(200)	33.09°	16.55°	5.410
3	(220)	47.52°	27.76°	5.407
4	(222)	56.29°	28.16°	5.416
Average				5.411

annealed products at 600°C - 800°C (ZnO:S) are $a = 3.25 \text{ \AA}$ (paek#1) and $c = 5.20 \text{ \AA}$ (peak#2) and $c/a = 1.6$. These obtained values compared well with the values published in literature (ZnS: $a = 5.41 \text{ \AA}$, ZnO: $a = 3.25 \text{ \AA}$, $c = 5.21 \text{ \AA}$ and $c/a = 1.6$).

Table 3.4 The assigned (h k l) from non-cubic crystal group II (ZnO:S) $\frac{1}{d^2} = \frac{4}{3} \left(\frac{h^2+hk+k^2}{a^2} \right) + \frac{l^2}{c^2} = \frac{4\sin^2\theta}{\lambda^2}$.

Peak No.	2θ	I/I_0	$\sin^2\theta$	d(nm)	(h k l)
1	31.770	0.57	0.075	2.813	100
2	34.420	0.44	0.088	2.602	002
3	36.250	1.00	0.097	2.475	101
4	47.540	0.23	0.162	1.910	102
5	56.600	0.32	0.225	1.624	103
6	62.860	0.29	0.272	1.477	200
7	66.380	0.40	0.300	1.407	112
8	67.930	0.23	0.312	1.378	201
9	69.100	0.11	0.322	1.358	004

Table 3.5 Calculated lattice parameters for XRD group II (ZnO:S) $\frac{1}{d^2} = \frac{4}{3} \left(\frac{h^2+hk+k^2}{a^2} \right) + \frac{l^2}{c^2} = \frac{4\sin^2\theta}{\lambda^2}$.

Peak No.	2θ	$\sin^2\theta$	(h k l)	a	c	$h^2 + hk + k^2$	l^2
1	31.770	0.075	100	3.248	-	1	-
2	34.420	0.086	002	-	5.205	-	4
3	36.250	0.097	101	-	-	-	-
4	47.540	0.163	102	-	-	-	-
5	56.600	0.225	103	-	-	-	-
6	62.860	0.272	200	3.410	-	4	-
7	66.380	0.299	112	-	-	-	-
8	67.930	0.312	201	-	-	-	-
9	69.100	0.322	004	-	5.431	-	16
Average				3.329	5.318	c/a	1.597

3.3 Thermal gravitational analysis (TGA)

TGA technique was done to determine the mass change with temperature in the range 0°C - 800°C with heating rate of 10°C/min in air. From TGA data

the phase transition occurs around 600°C. The structure of final product is almost stabilized at 800°C as shown in Figure 3.5.

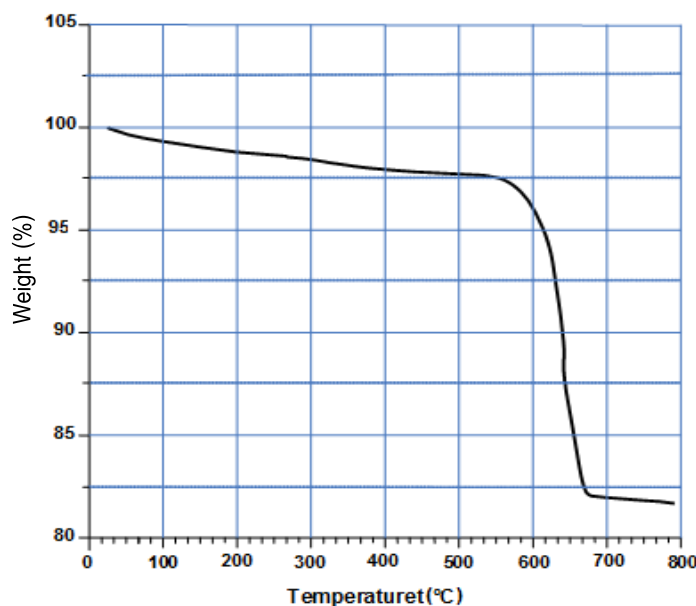


Figure 3.5 TGA data of ZnS annealing.

From TGA data together with the XRD diffraction pattern, it can be concluded that the nanocrystal sample has transformed from zinc-blend crystal structure of ZnS to wurtzite ZnO:S at the temperature around 600°C. It is noteworthy that some discrepancies in the transition temperature may arise from the fact that the temperature in hot air oven used in this work was not well calibrated.

3.4 Scanning electron microscope (SEM)

The JEOL scanning electron microscope model JSM-6400 was used to study the morphology of S doped ZnO prepared by oxidative annealing. The SEM can give the information about the morphology and surface of crystals. From the SEM micrographs of ZnS powder and annealing products at 200°C - 800°C with magnification 10000X, are shown in Figure 3.6. The differences in surface morphology

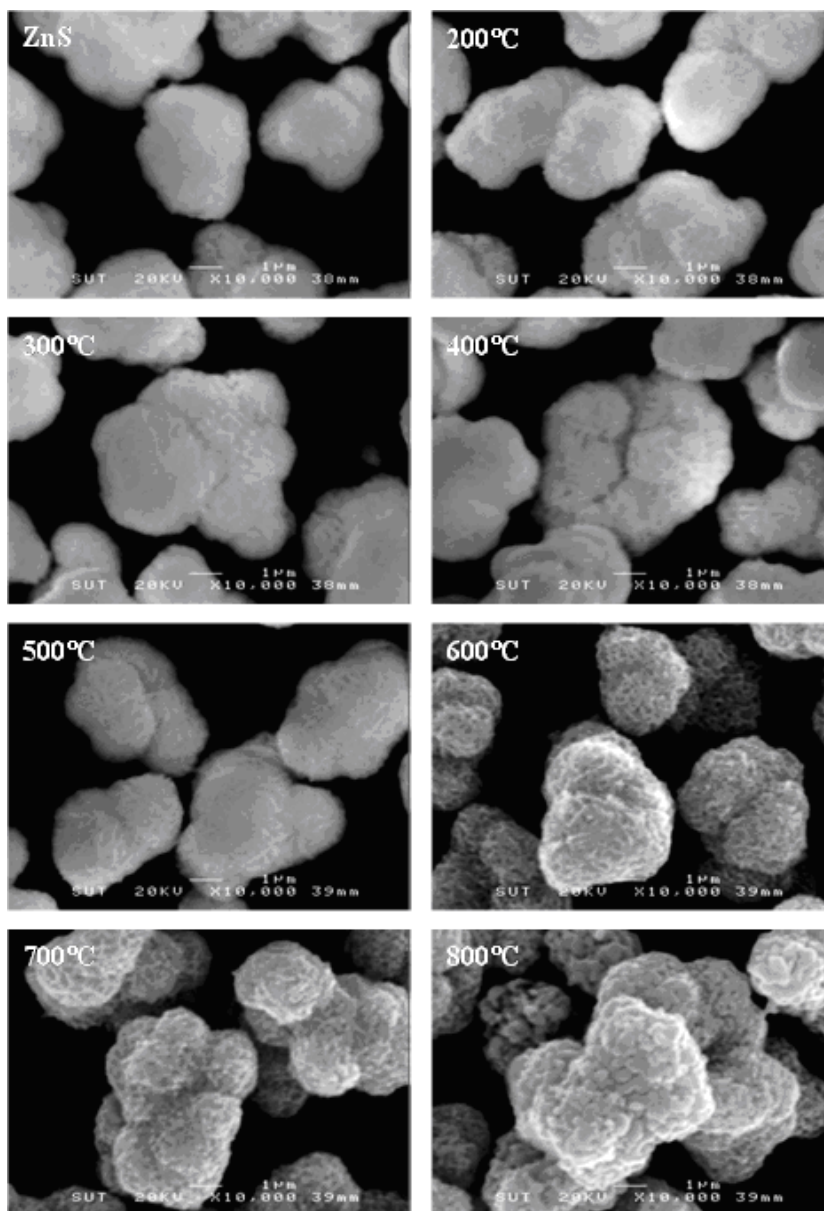


Figure 3.6 SEM images of ZnS powder and annealing products at 200°C - 800°C.

of powder products annealed at different temperatures can be seen. It is evidence that the powder morphology has changed with the annealing temperature due to thermal roughening. The S-doped ZnO samples appear to have very rough surfaces compared to ZnS samples. Noting that the powder size observed by SEM is about 1 μm which is the cluster size of nanocrystals not the crystal grain size. (A powder grain is, in itself, polycrystals.)

3.5 Energy Dispersive Spectroscopy (EDS)

Energy Dispersive Spectroscopy was used to analyze the composition of the product to ensure that S is left in the ZnO:S product. EDS spectra of ZnS powder, annealing products at 600°C and 800°C are shown in Figure 3.7.

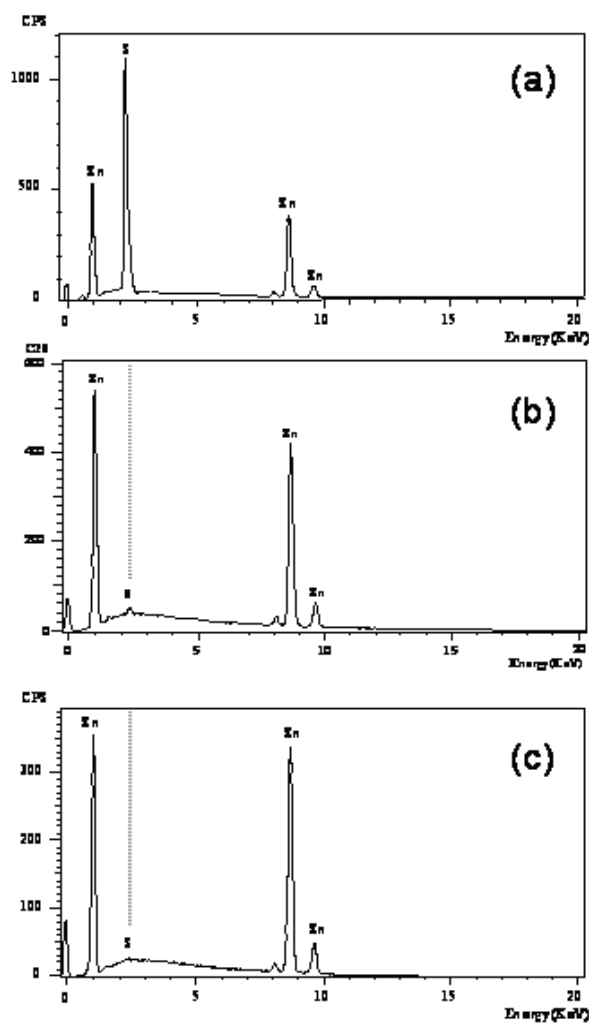


Figure 3.7 EDS spectra of (a) ZnS powder, (b) 600°C S-doped ZnO powder and (c) 800°C S-doped ZnO powder.

After annealing products at 200°C - 800°C some trace of sulfide can be seen by EDS in the annealing products. It was estimated that the sulfur concentration of the sample ZnS annealed at 600°C, is about 0.5% and at 800°C the sulfur concentration is 0.25%. The sulfur concentrations measured by EDS are reported

in Table 3.6. The result suggests that ZnO:S nanocrystals can be formed by oxidative annealing.

Table 3.6 The sulfur concentrations in annealing products as determined by EDS.

Sample	A	B	C	D	E	F	G	H
Annealing temperature (°C)	RT	200	300	400	500	600	700	800
Sulfur atoms (cps)	1100	1346	1351	1400	1005	100	25	27
Zinc atoms (cps)	550	631	646	670	461	1141	492	335
Ratio of S:Zn	2.07:1	2.13:1	2.09:1	2.08:1	2.05:1	0.10:1	0.09:1	0.05:1
Sulfur concentrate (%)	100	100	100	100	100	0.50	0.45	0.25

3.6 Transmission electron microscope (TEM)

Transmission electron microscope was used to observe the microstructure of the annealed products. The low-magnification image of the ZnS powder and annealing products nanoparticle was illustrated in Figures 3.8 - 3.10.

From the TEM micrographs it can be seen that showed that the annealing products at 200°C - 500°C are nanocrystals with quite uniform particle size about 30 - 50 nm. After the structural transition temperature, the particle size is increased to 50 - 100 nm. The crystal larger than 100 nm can be seen at the temperature of 800°C possibly due to the fact that nanocrystals can be recrystallized

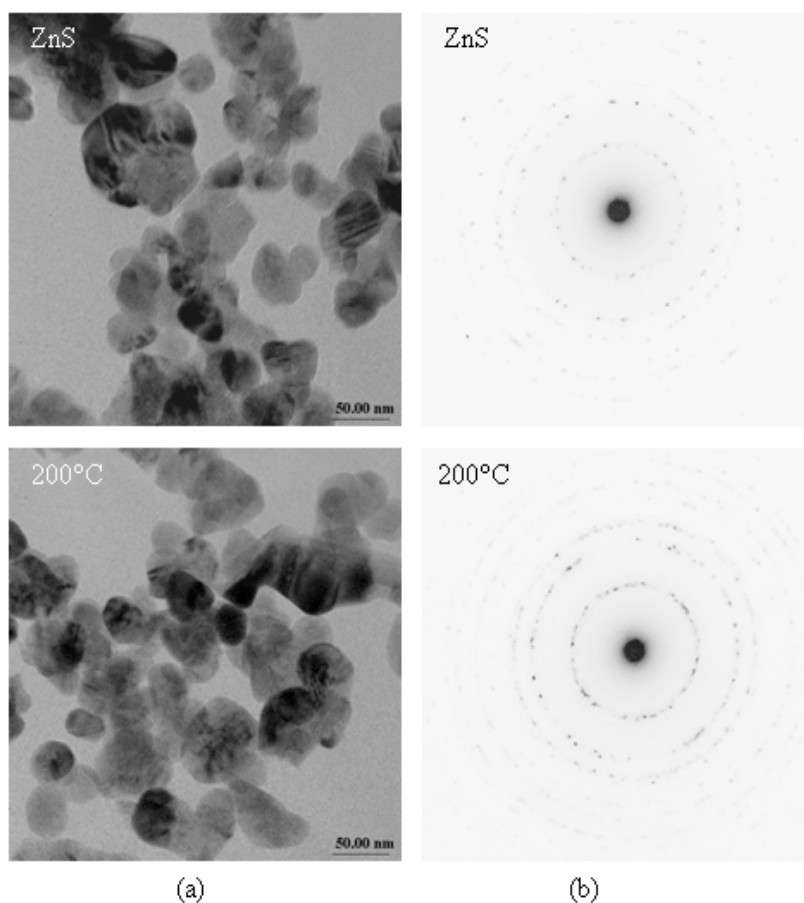


Figure 3.8 TEM images of ZnS powder and annealing product at 200°C and (b) selected area electron diffraction patterns of ZnS powder and annealing product at 200°C.

and merged together at this temperature. These observations are consistent with the XRD result. The corresponding selected area electron diffraction (SEAD) patterns are shown in Figures 3.8 - 3.10. The index the polycrystalline ring observed by SEAD a calibration with Si crystal has been done. Figure 3.11 shows a reverse color image of SEAD pattern taken from annealed product at 200°C and 600°C. The indexed rings agree well with XRD pattern of zincblend ZnS and wurtsite ZnO respectively. From SEAD patterns the structural transition temperature at 600°C suggested by XRD can be confirmed. This result is consistent with the finding of Lu et al. (Lu et al., 2004) on the oxidation of ZnS nanoparticles in to

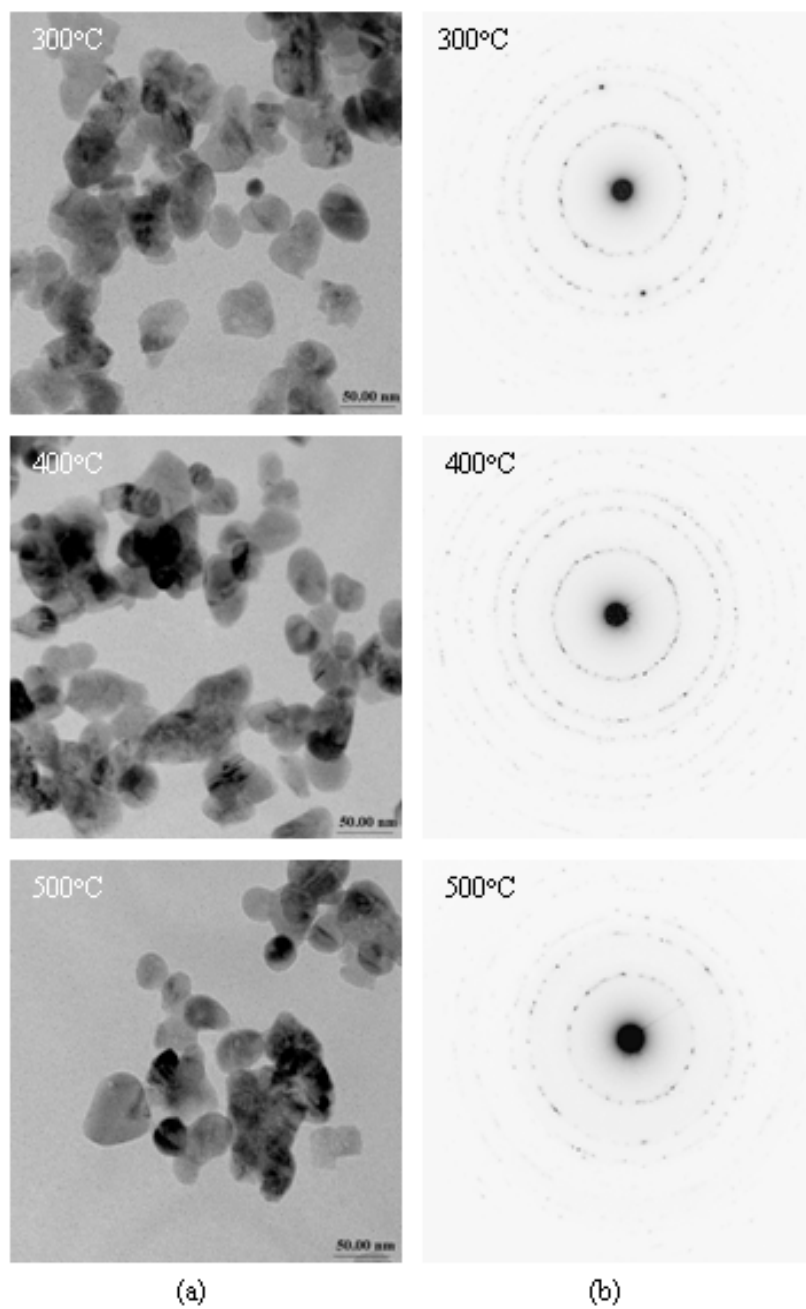


Figure 3.9 (a) TEM images of annealing products at 300°C, 400°C and 500°C and (b) selected area electron diffraction patterns of annealing products at 300°C, 400°C and 500°C.

ZnO nanoparticles.

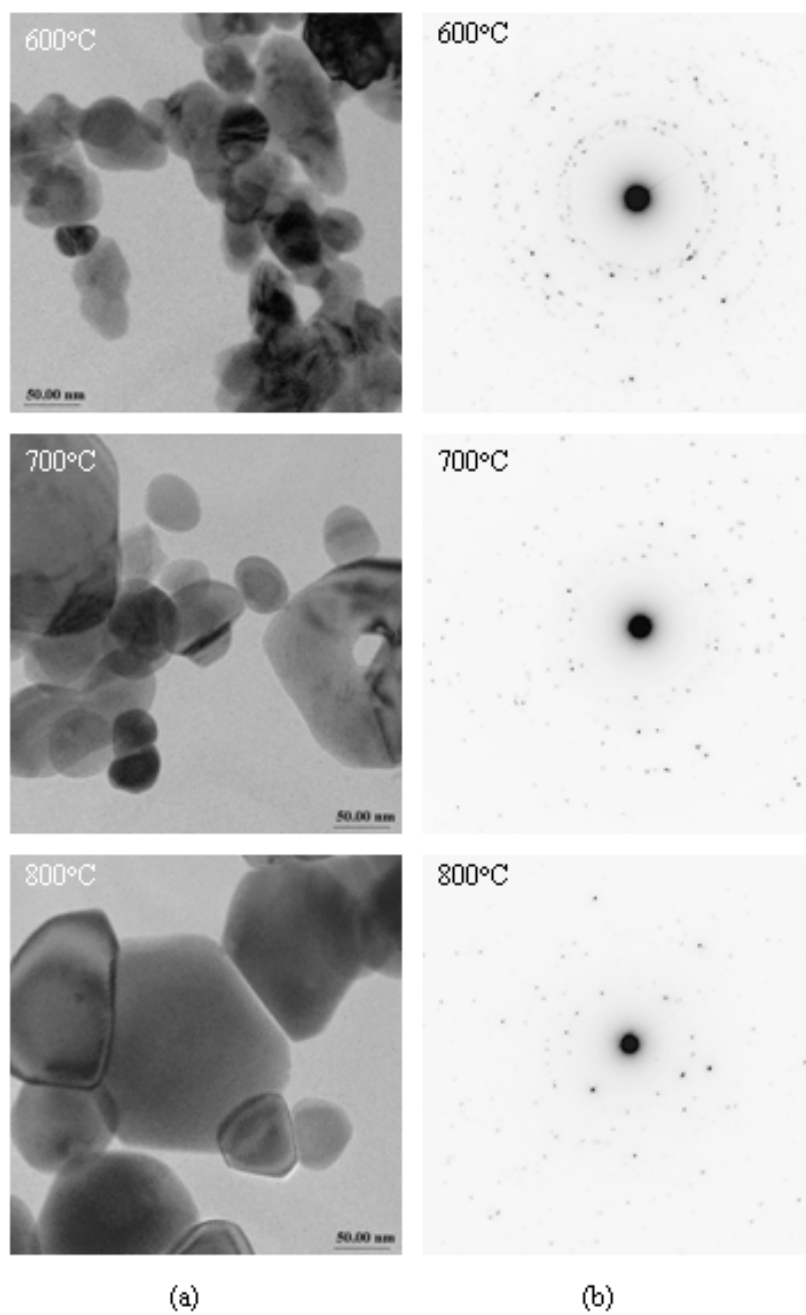


Figure 3.10 (a) TEM images of annealing products at 600°C, 700°C and 800°C and (b) selected area electron diffraction patterns of annealing products at 600°C, 700°C and 800°C.

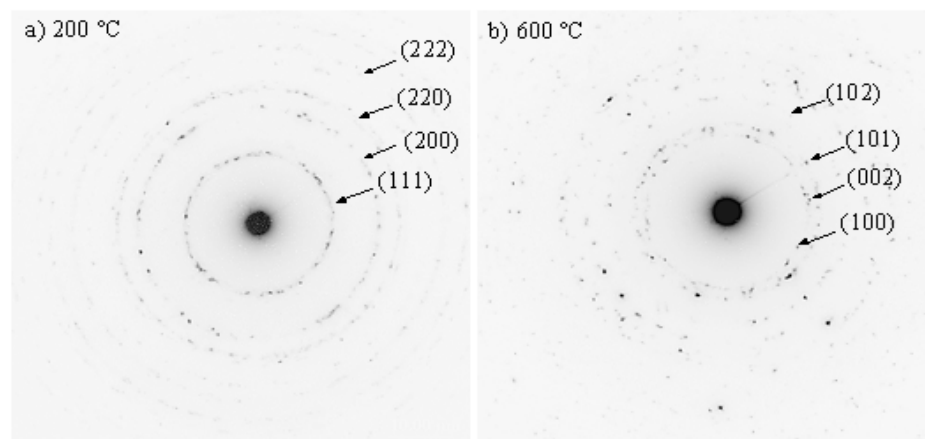


Figure 3.11 The indexed electron diffraction patterns of (a) annealing product at 200°C (ZnS) and (b) 600°C (ZnO:S).

CHAPTER IV

XAS STUDY OF SULFUR DOPED ZINC OXIDE

In the last chapter the microstructural study of nanocrystalline annealed products using XRD, SEM, EDS and TEM suggest that there is a certain amount of sulfur in the wurtzite framework of ZnO:S. This brought in the question, whether sulfur substitute oxygen and form $\text{ZnS}_x\text{O}_{1-x}$ alloys as desired or not. The question can not be answered by standard characterization techniques used in chapter III. Luckily, XAS facility was accessible to us through the user beamtime allocated by SLRI. It will be shown in this chapter that XAS can give a clear picture of local structure around S dopants in ZnO:S nanocrystals, and provide a conclusive answer to the question raised above.

4.1 XAS measurement of sulfur doped ZnO

XAS spectra were collected at the XAS facility (BL-8) of the Siam Photon Laboratory, Synchrotron Light Research Institute, Nakhon Ratchasima, with the storage ring running at 1.2 GeV and beam current of 80 - 120 mA during the measurement. XAS measurement was performed in the transmission mode using Si (111) monochromator. The x-ray transparent Kapton® tape was used to mount the samples. The spectra were collected for the *K*-edges of Zn (9569 eV) and S (2472 eV) in ZnO:S nanocrystal samples. Both XANES and EXAFS were collected an energy step of 1.0 eV.

4.2 XANES Analysis

XANES can provide basic information about the local structure around the specific absorbing atoms. The measured Zn and S K-edges XANES spectra of ZnO:S are shown in Figure 4.1 and 4.2, respectively, in comparison with either ZnO or ZnSO₄ and ZnS.

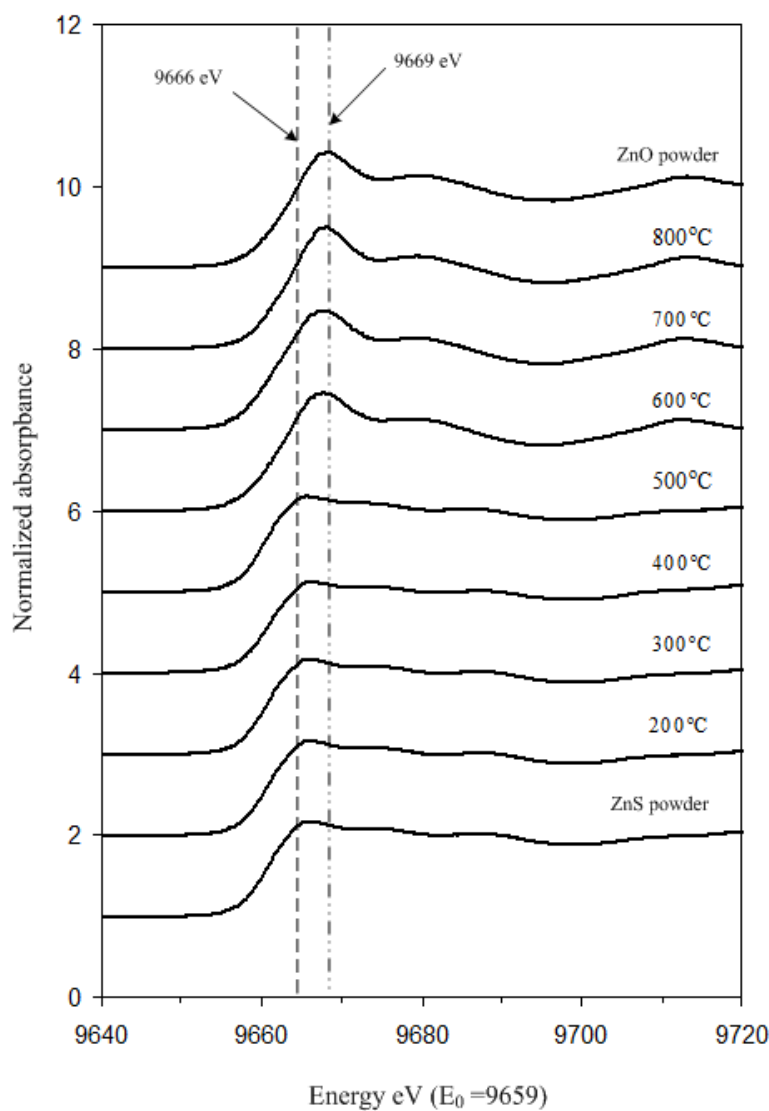


Figure 4.1 Zn *K*-edge XANES spectra of in ZnO:S annealed at different temperatures compared with ZnO and ZnS.

From XANES Zn *K*-edge finger print, it can be conclude that the local

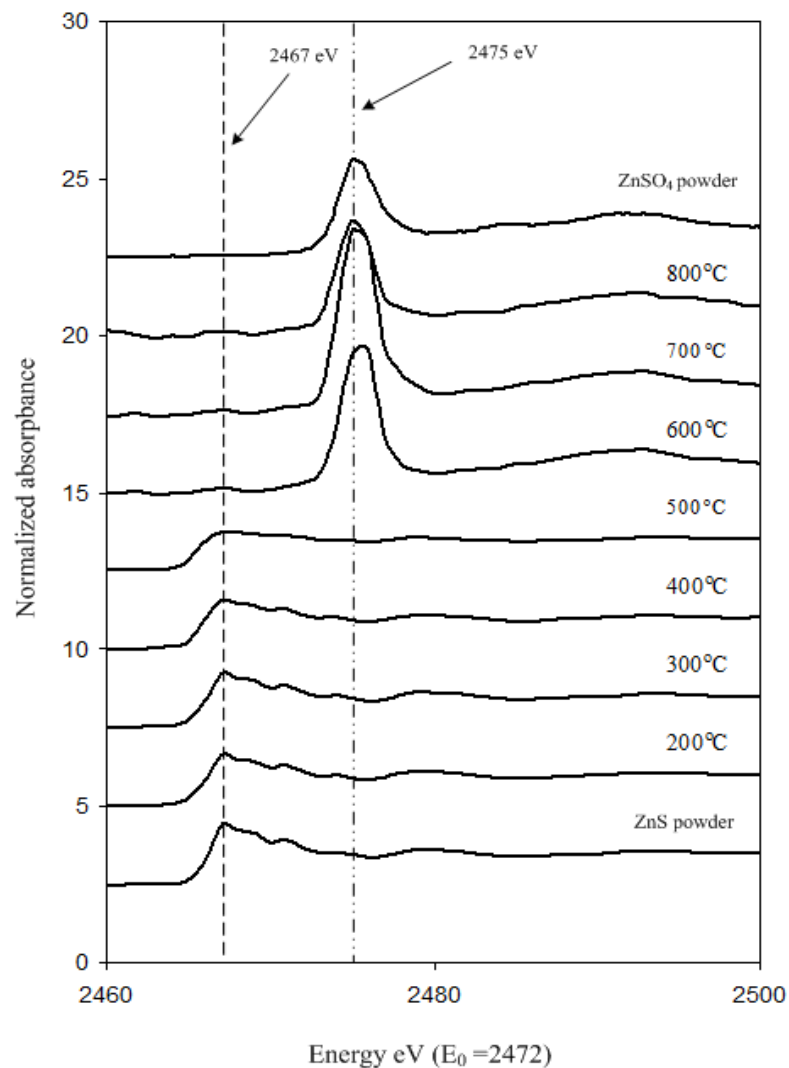


Figure 4.2 S *K*-edge XANES spectra of in ZnO:S annealed at different temperatures compared with ZnSO₄ and ZnS.

structure around Zn atoms in ZnO:S sample above the transition temperature is wurtzite ZnO-like as indicated by XRD and TEM. On the other hand, XANES S *K*-edge shows, unambiguously, that the local structure around S atoms in ZnO:S sample above the transition temperature is ZnSO₄-like. Therefore, the assumption of ZnS_xO_{1-x} alloys formation is not consistent with the characterization of our oxidative annealed ZnO:S samples. Since trace of ZnSO₄ is undetected by XRD or

SEAD patterns, even if subnano-domains ZnSO_4 is formed it can not be observed anyway. EXAFS result confirms that S should be left in the form of $(\text{SO}_4)^{2-}$ on the surface of ZnO:S nanocrystals rather than in the form of subnano-domains ZnSO_4 .

4.3 EXAFS Analysis

The EXAFS data was analyzed using ATHENA software to get the EXAFS structures. The k^2 -weighted spectrum over the k -range of 2.0 - 8.0 \AA^{-1} was done for curve fitting. The structural parameters can be obtained from direct EXAFS fittings. Figure 4.3 shows k^2 -weighted Zn K -edge EXAFS spectra: ZnS powder, annealing products at 200°C - 800°C, and pure ZnO powder. Figure 4.4 shows the corresponding EXAFS spectra in real space. It can be seen that the spectra can be separated into two groups. The first group: there are five spectrums, the spectra of ZnS powder and annealing products at 200°C - 500°C. The second group the annealing products at 600°C - 800°C and pure ZnO. As shown in Figures 4.3 and 4.4, the first group can be fitted very well with ZnS structure while the second group can be fitted with ZnO structure.

Shown in Figure 4.5 are k^2 -weighted S K -edge EXAFS spectra: ZnS powder, annealing products at 200°C - 800°C, and pure ZnSO_4 powder. Figure 4.6 shows the corresponding EXAFS spectra in real space. The EXAFS spectra can be separated into two groups. The first group, similar to the Zn K -Edge: there are five spectrums, the spectra of ZnS powder and annealing products at 200°C - 500°C. However, the second group, the annealing products at 600°C - 800°C can be fitted well with $(\text{SO}_4)^{2-}$ model. Thus the possibility to obtain wurtzite $\text{ZnS}_x\text{O}_{1-x}$ alloys by oxidative annealing is eliminated.

To take a closer look, the EXAFS oscillations of ZnO:S spectra in Figure 4.5

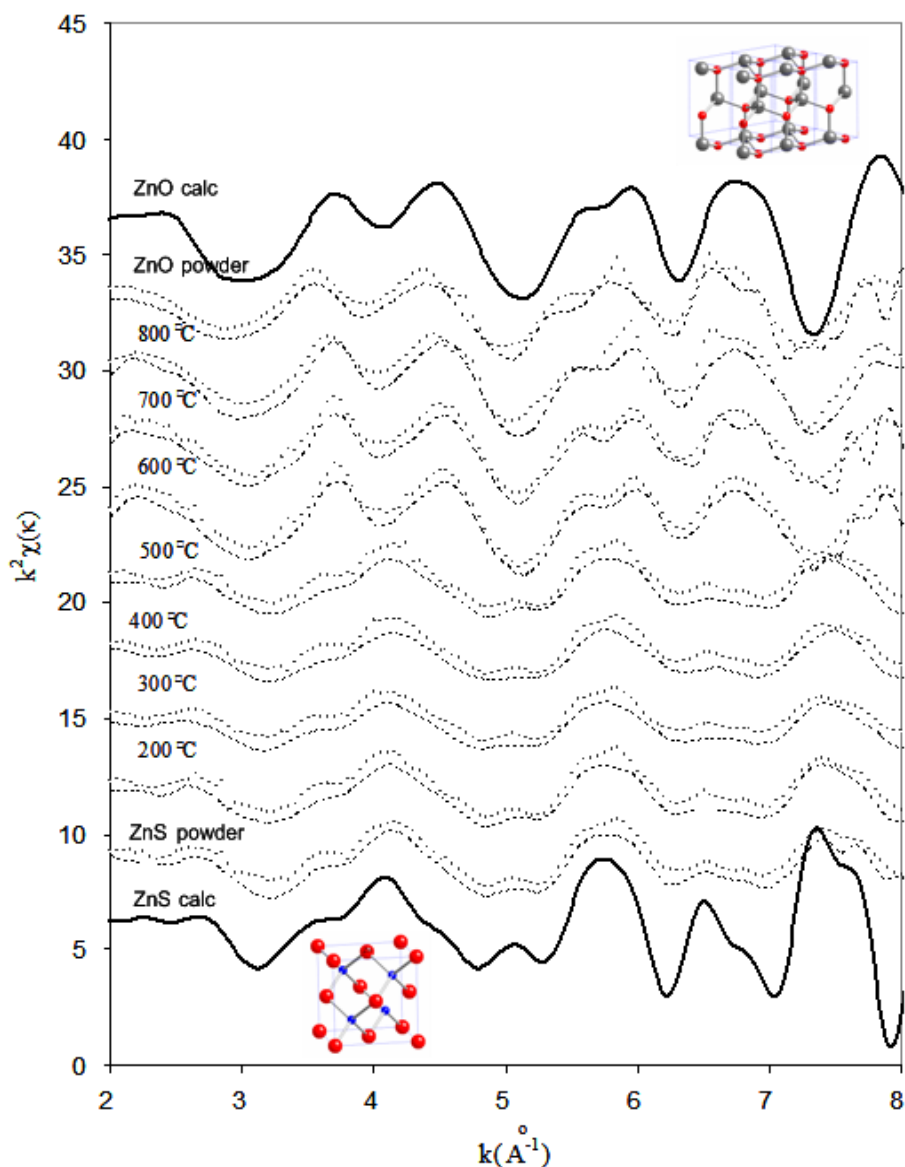


Figure 4.3 k^2 -weighted Zn K -edge EXAFS spectra (dot lines): ZnS powder, annealing products at 200°C - 800°C, and pure ZnO powder. Fittings spectra are shown in dash lines. The FEFF-generated spectra are shown in solid lines.

have shorter periods compared to that of ZnSO_4 . The real space EXAFS spectra in Figure 4.6 suggest that S-O bonds in ZnO:S are about 1.5 Å, longer than that of S-O bonds in ZnSO_4 crystals. The fitting results of S-O bond-lengths in the samples are shown in Table 4.1.

With larger bond-lengths, compared to bulk ZnSO_4 , it is possible that

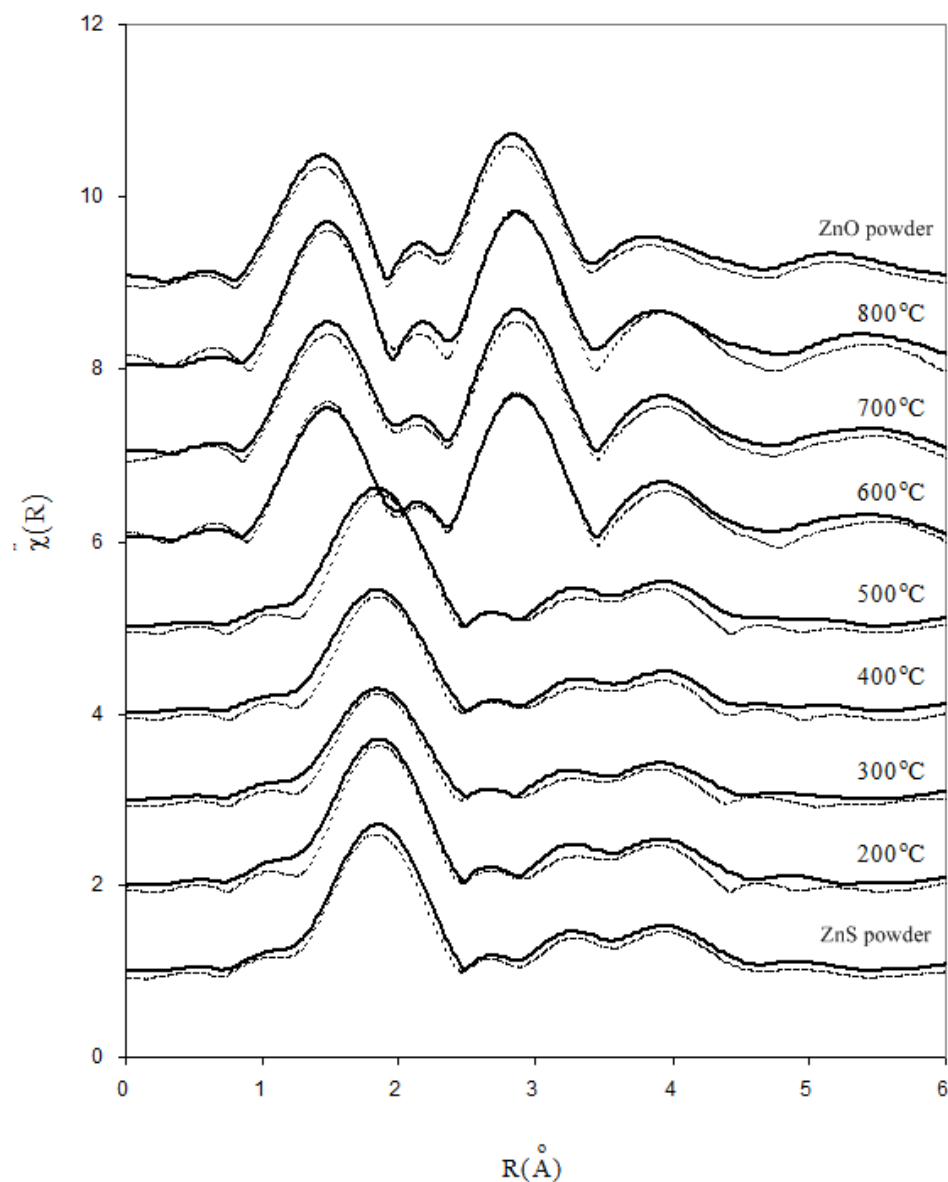


Figure 4.4 Real space Zn *K*-edge EXAFS spectra (solid): ZnS powder, annealing products at 200°C - 800°C, and pure ZnO powder. Fittings spectra are shown in dash lines.

$(\text{SO}_4)^{2-}$ would exist on the surface of ZnO:S by coordinate bonding to the surface Zn atoms, result in the saturation of dangling bonds.

This has demonstrated that XAS can give an unique point of view on the local structure around S dopants in ZnO:S nanocrystals which is unreachable by standard microstructure characterizations such as XRD or TEM.

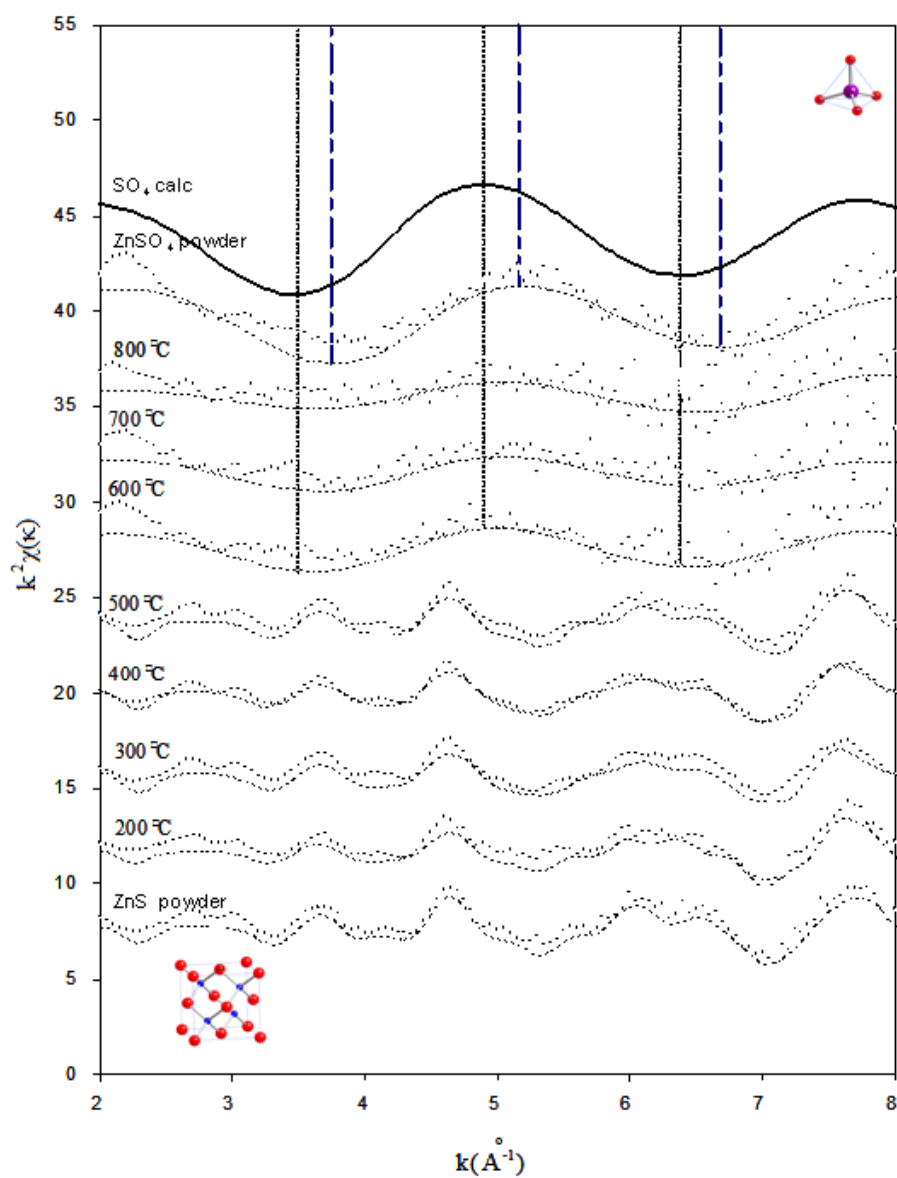


Figure 4.5 k^2 -weighted S K -edge EXAFS spectra (dot lines): ZnS powder, annealing products at 200°C - 800°C, and pure ZnSO₄ powder. Fittings spectra are shown in dash lines. The FEFF-generated (SO₄)²⁻ spectrum is shown in solid line.

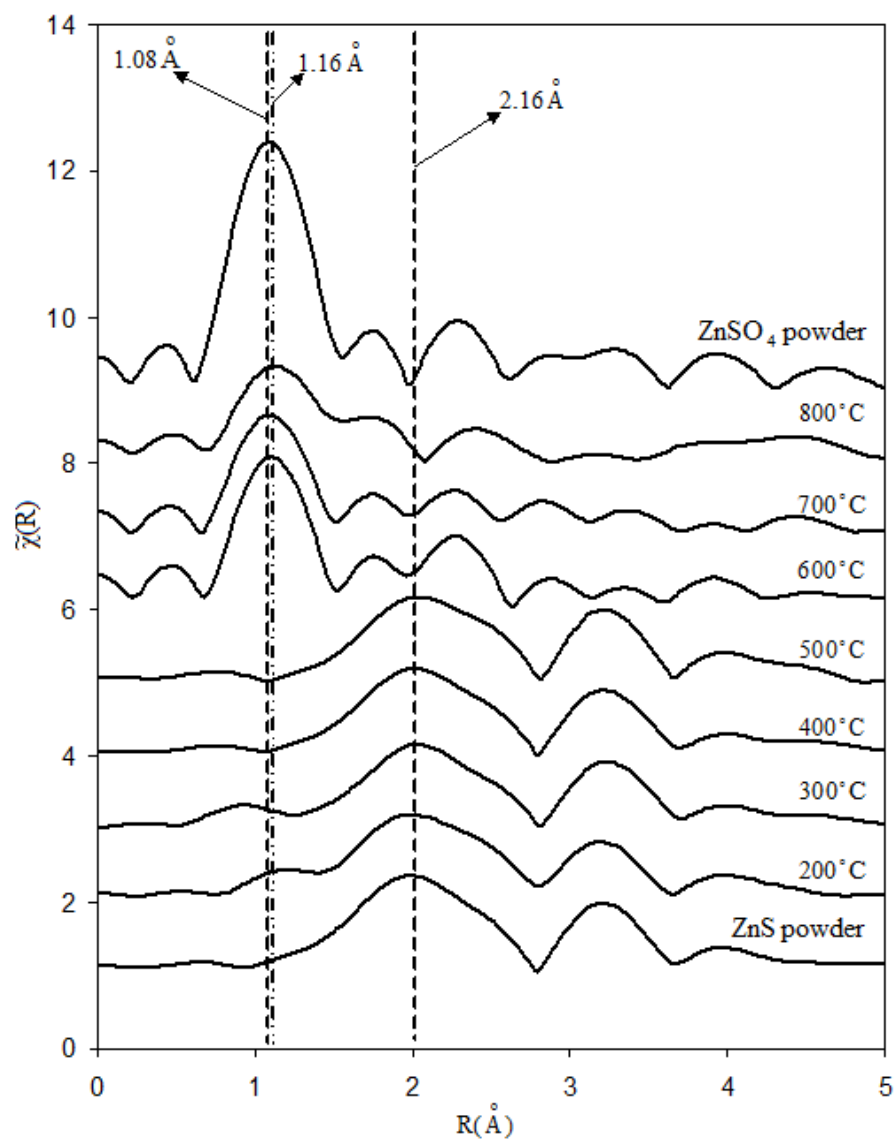


Figure 4.6 Real space S K -edge EXAFS spectra (solid): ZnS powder, annealing products at 200°C - 800°C , and pure ZnSO_4 powder.

Table 4.1 Results from the EXAFS fitting for S-O bonds in ZnO:S nanocrystals compared to ZnSO₄: R_0 is nearest neighbor shell distance, N is coordination number, σ^2 is Debye-waller factor, and R-factor is the residue.

Samples	R_0 (\AA)	σ^2 (\AA^2)	N	R-factor
ZnO:S 600°C	1.506 ± 0.05	0.291	4	0.010
ZnO:S 700°C	1.492 ± 0.10	0.274	4	0.009
ZnO:S 800°C	1.499 ± 0.07	0.081	4	0.175
ZnSO ₄	1.486 ± 0.09	0.655	4	0.005

CHAPTER V

CONCLUSIONS

In this thesis, it has been demonstrated that ZnO:S nanocrystals can be prepared by an economic method called oxidative annealing. Standard characterization techniques such as TGA, XRD, SEM, EDS and TEM were used for microstructural studies of the synthesis nanocrystals.

It was found that the zincblend-ZnS to wurtzite-ZnO structural transition temperature occurs around 600°C during the annealing in atmosphere. Above the transition temperature the ZnS nanocrystals can be oxidized and recrystallized into ZnO:S nanocrystals. A small amount of sulfur atoms (0.25 - 1%) can be found in ZnO:S annealing products. This gave rise to the speculation that weather II - VI $\text{ZnS}_x\text{O}_{1-x}$ alloys can be synthesized by oxidative annealing or not.

XAS was utilized as a key characterization technique to give a unique answer. While Zn *K*-edge XAS measurements give similar result to XRD and TEM that is most of Zn in ZnO:S are in wurtzite matrix as expected, the S *K*-edge XAS give a remarkable result : the majority of S atoms reside in $(\text{SO}_4)^{2-}$ structural form possibly attached to Zn surface atoms of ZnO:S nanocrystals. This finding by XAS can not be reached by other techniques such as XRD or TEM due to limiting resolutions. Thus, the outstanding performance of XAS to resolve the sub-nano structure in nanocrystal materials can be pronounced over standard characterization techniques, once again.

REFERENCES

REFERENCES

- Ankudinov, A. L., Ravel, B., Rehr, J. J., and Conradsau, S. D. (1998). Real-space multiple-scattering calculation and interpretation of x-ray-absorption near-edge structure. **Phys. Rev.** B58: 7565.
- Fong, C. Y., Weber, W., and Phillips, J. C. (1976). Violation of Vegard's law in covalent semiconductor alloys. **Phys. Rev.** B14(12): 5387-5391.
- Gorla, C. R., Emanetoglu, N. W., Liang, S., Mayo, W. E., and Lu, Y. (1999). Structural, optical, and surface acoustic wave properties of epitaxial ZnO films grown on (0112) Sapphire by metalorganic chemical vapor deposition. **J. Appl. Phys.** 84(5): 2595-2602.
- Gupta, V. and Mansingh, N. (1996). Influence of postdeposition annealing on the structural and optical properties of sputtered zinc oxide film. **J. Appl. Phys.** 80(2): 1063-1073.
- Hammond, C. (1992). **Introduction to crystallography.** Oxford University Press: Royal Microscopical Society.
- Jagadish, C. and Pearton, S. (2006). **Zinc Oxide Bulk, Thin Films and nanostructures.** Oxford: Elsevier.
- Kawai, J. (2000). **Absorpyion Techniques in x-ray Spectrometry, Encyclopedia of Analytical chemistry.** New York: John Wiley & Sons. Inc.
- Koningsberger, D. C. and Prins, R. (1998). **X-ray Absorption:Principles, Ap-**

plications, Techniques of EXAFS, SEXAFS and XANES. New York: John Wiley & Sons. Inc.

Lu, H., Chu, S. Y., and Tan, S. S. (2004). The characteristics of low-temperature-synthesized ZnS and ZnO nanoparticles. **J. Crystal Growth.** 269: 385-391.

Makino, T., Sgawa, Y., Kawasaki, M., Ohtomo, A., Shiroki, R., and Tamura, K. (2001). Band gap engineering based on $Mg_xZn_{1-x}O$ and $Cd_yZn_{1-y}O$ ternary alloys films. **Appl. Phys. Lett.** 78(9): 1237-1239.

Moore, G. E. (1965). Cramming more components onto integrated circuits. **Electronics.** 38: 8.

Rehr, J. J. and Albers, R. C. (2000). Theoretical approaches to x-ray absorption fine structure. **Rev. Mod. Phys.** 72: 621.

Smith, M. F., Onkaw, D., Na-phattalung, N., Limpijumnong, S., and Rujirawat, S. (2007). Identification of bulk and surface sulfur impurities in tio_2 by synchrotron x-ray absorption near edge structure. **Appl. Phys. Lett.** 91: 142107-142103.

Umebayashi, T., Yamaki, T., Itoh, H., and Asai, K. (2002). Band gap narrowing of titanium dioxide by sulfur doping. **Appl. Phys. Lett.** 81(3): 454-456.

William, D. B. and Carter, C. B. (1996). **Transmission Electron Microscopy: A Textbook for Materials Science.** Plenum Press, New York.

Wong, E. M. and Searson, P. C. (1999). ZnO quantum particle thin films fabricated by electrophoretic deposition. **Appl. Phys. Lett.** 74(20): 2939-2941.

Yang, H., Holloway, P. H., and Ratna, B. B. (2003). Photoluminescent and electroluminescent properties of Mn-doped ZnS nanocrystals. **J. Appl. Phys.** 93(1): 586-592.

APPENDIX

Scanning electron microscope study of sulfur doped ZnO powder

Rattiya Ngonchaiyaphum^{1*}, Saroj Rujirawat^{1,2}

¹School of Physics, Institute of Science, Suranaree University of Technology, Nakhon Ratchasima Thailand

²National Synchrotron Research Center, Nakhon Ratchasima Thailand

*Corresponding author, e-mail: rattiya@g.sut.ac.th

Abstract

We used scanning electron microscope to examine sulfur doped ZnO powder. To explore the possibility of alloying ZnS and ZnO, the sulfur doped ZnO powder was prepared by oxidative annealing, with ZnS powder as the starting material. The annealing products were characterized by x-ray diffraction (XRD), thermal gravimetric (TGA), and scanning electron microscopy (SEM). It was found that the structural transformation of ZnS into ZnO occurs around 650 °C. From SEM observation, the powder morphology was drastically changed possibly due to Oswald ripening. Energy dispersive spectroscopy (EDS) indicates that the ZnO products contain small amount of sulfur. However, the exact location of sulfur atoms in ZnO is still unknown.

Background

ZnO is a wide bandgap compound semiconductor ($E_g=3.37$ eV). It is one of the promising materials for low-voltage luminescence and short wavelength light emitter [1]. ZnO in powder form are used in a variety of applications, such as UV light emitter, UV absorption and cosmetic powder [2].

ZnS is also a wide bandgap compound semiconductor ($E_g=3.54$ eV). ZnS has received much attention due to its excellent properties, such as large band gap energy, direct recombination and resistance to high electric field. ZnS is also a well known phosphor material with various luminescence properties [3].

While p-type doping of ZnO was found to be problematic, ZnS can be doped as both n-type and p-type, which is unusual for the II-IV semiconductors. Therefore, alloys between ZnO and ZnS may possess some interesting doping ability. In this work, we aim to explore the possibility of alloying ZnS and ZnO using oxidative annealing process [4]. SEM was used as a main characterization tool to investigate the microstructure of the annealing products.

Materials and Methods

S-doped ZnO powder was prepared by oxidative annealing of ZnS powder (high purity grade, 99.99%) in atmosphere at 200 - 800 °C for 2 hours. The annealing products were characterized by powder x-ray diffraction (XRD), thermal gravimetric (TGA), scanning electron microscopy

(SEM), and energy dispersive spectroscopy (EDS).

Results, Discussion and Conclusion

The powder XRD patterns of ZnS powder and annealing products at 200, 500, 600, and 800 °C. are shown in Fig. 1(a)-(e) respectively. It can be seen that the annealing product at temperatures 500 °C and lower still have ZnS structure. The structural transformation was seen at the temperature 600 °C. At 800 °C, XRD shows that the product is almost pure ZnO. The exact transformation temperature was determined by TGA to be around 650 °C. It is noteworthy that the discrepancies in temperatures may be arisen from the fact that the temperature in the hot air oven used in this work was not well calibrated.

Figure 2 shows SEM images of ZnS powders and annealing product at 800 °C. It can be seen that the thermal roughening may change the powder morphology, possible via Oswald ripening during the oxidation process.

EDS was used to analyze the composition of the product. As shown in Fig. 3, some trace of sulfur can be seen in the annealing product. It was estimated that the sulfur concentration of 600 °C and 800 °C annealing products are about 1 %, 0.25% respectively. Therefore it may be possible to dope ZnO with S. Nevertheless, the exact position of sulfur in ZnO lattice is still be unknown. More sophisticate analytical technique such as synchrotron x-ray absorption spectroscopy [5] may be used to provide the final answer in further

investigation.

Acknowledgements

R.N. would like to thank the school of physics, institute of science, and the center of science and technology equipment (CSTE) Suranaree University of Technology (SUT), for all supports.

References

1. Zhong J., Kitai A.H., Mascher P. and Puff W. The effect of processing conditions on point defects and luminescence centers in ZnO. *J. Electrochem. Soc.* 1993, 140: 3644.
2. Pearton SJ, Norton DP, Ip K, Heo YW, Steiner T. Recent progress in processing and properties of ZnO. *Superlattice Microst* 2003, 34: 3-32.
3. Lu H.Y., Chu S.Y., Tan S.S. The characteristics of low-temperature synthesized ZnS and ZnO nanoparticles. *J Crystal Growth* 2004, 269: 385-391.
4. Umegashi T., Yamaki T., Itoh H., Asao K. Band gap narrowing of titanium dioxide by sulfur doping. *Appl. Phys. Lett.* 2002, 81: 454-456.
5. Smith M.F., Setwong K., Tongpool R., Onkaw D., Na-phattalung S., Limpijumng S., Rujirawat S. Identification of bulk and surface sulfur impurities in TiO₂ by synchrotron x-ray absorption near edge structure. *Appl. Phys. Lett.* 2007, 91: 142107.

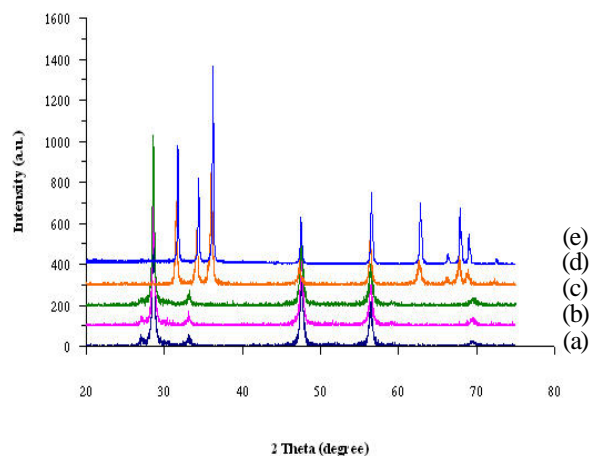


Figure 1 XRD patterns of (a) ZnS powder; (b) annealing products at 200 °C; (c) 500 °C; (d) 600 °C; (e) 800 °C

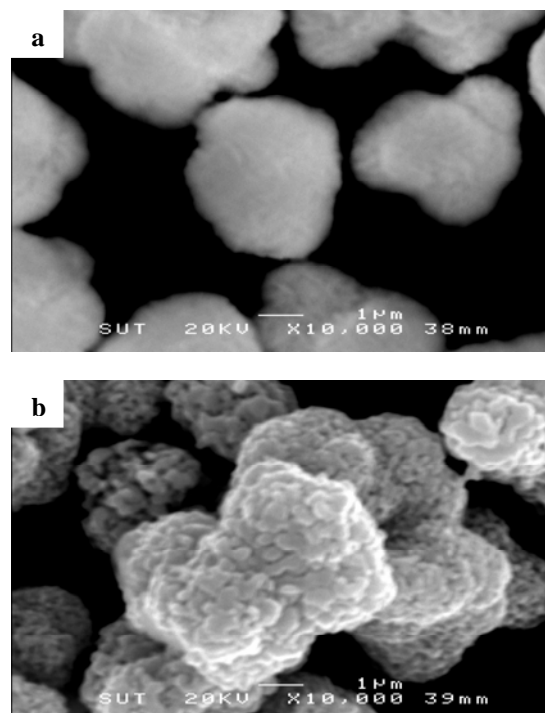
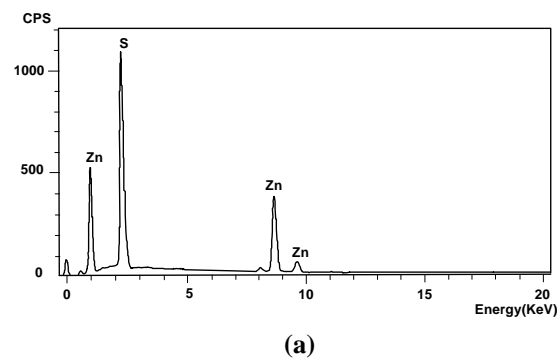


Figure 2 SEM micrographs of

(a) ZnS powder

(b) S-doped ZnO powder (800°C)



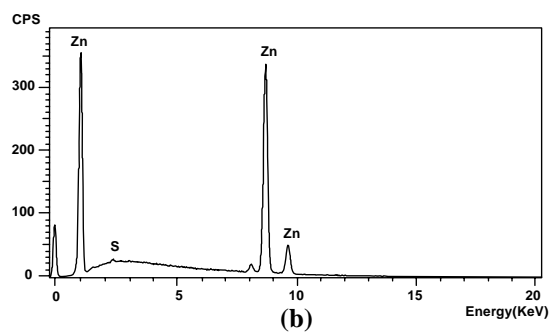


Figure 3 EDS Spectra of
(a) ZnS powder

(b) S-doped ZnO powder (800°C)

CURRICULUM VITAE

NAME: Rattiya Ngonchayaphum.

GENDER: Female.

NATIONALITY: Thai.

DATE OF BIRTH: February 25, 1970.

PLACE OF BIRTH: Nakhon Ratchasima, Thailand.

EDUCATIONAL BACKGROUND:

1989 - 1992 Naresuan University, Pithsanuloke, Thailand

Bachelor of Science (Physics)

2006 - present Currently enrolling in

Master degree majoring in Physics,

School of Physics, Institute of Science,

Suranaree University of Technology,

Nakhon Ratchasima, Thailand